




# A dual role for cell plate-associated PI4K $\beta$ in endocytosis and phragmoplast dynamics during plant somatic cytokinesis

Feng Lin<sup>1</sup> , Praveen Krishnamoorthy<sup>1</sup>, Veit Schubert<sup>2</sup> , Gerd Hause<sup>3</sup>, Mareike Heilmann<sup>1</sup> & Ingo Heilmann<sup>1,\*</sup> 

## Abstract

Plant cytokinesis involves membrane trafficking and cytoskeletal rearrangements. Here, we report that the phosphoinositide kinases PI4K $\beta$ 1 and PI4K $\beta$ 2 integrate these processes in *Arabidopsis thaliana* (*Arabidopsis*) roots. Cytokinetic defects of an *Arabidopsis pi4k $\beta$ 1 pi4k $\beta$ 2* double mutant are accompanied by defects in membrane trafficking. Specifically, we show that trafficking of the proteins KNOLLE and PIN2 at the cell plate, clathrin recruitment, and endocytosis is impaired in *pi4k $\beta$ 1 pi4k $\beta$ 2* double mutants, accompanied by unfused vesicles at the nascent cell plate and around cell wall stubs. Interestingly, *pi4k $\beta$ 1 pi4k $\beta$ 2* plants also display ectopic overstabilization of phragmoplast microtubules, which guide membrane trafficking at the cell plate. The overstabilization of phragmoplasts in the double mutant coincides with mislocalization of the microtubule-associated protein 65-3 (MAP65-3), which cross-links microtubules and is a downstream target for inhibition by the MAP kinase MPK4. Based on similar cytokinetic defects of the *pi4k $\beta$ 1 pi4k $\beta$ 2* and *mpk4-2* mutants and genetic and physical interaction of PI4K $\beta$ 1 and MPK4, we propose that PI4K $\beta$  and MPK4 influence localization and activity of MAP65-3, respectively, acting synergistically to control phragmoplast dynamics.

**Keywords** Cell division; cell plate; clathrin-mediated endocytosis, phosphoinositides; mitogen-activated protein kinase 4

**Subject Categories** Membrane & Intracellular Transport; Plant Biology

**DOI** 10.15252/emboj.2018100303 | Received 19 July 2018 | Revised 29 November 2018 | Accepted 4 December 2018 | Published online 7 January 2019

**The EMBO Journal (2019) 38: e100303**

## Introduction

Cytokinesis is the final step of cell division to separate a mother cell into two daughter cells, and of fundamental importance both in animals and in plants. In animals, cytokinesis is characterized by

the formation of the cleavage furrow and contractile ring (Glotzer, 2001). The cleavage furrow is a membrane barrier dividing the cytoplasm of the mother cell onto the daughter cells, whereas the contractile ring, consisting of actin and myosin, pulls the cleavage furrow inward to isolate the daughter cells. In contrast, cytokinesis in plant cells adopts a specialized strategy because of the presence of plant cell walls and involves the formation of the cell plate as a plant-specific membrane compartment for cell division (Jürgens, 2005; McMichael & Bednarek, 2013). In late anaphase/early telophase, the cell plate initiates between a mirrored array of microtubules, the phragmoplast, which provides guidance to membrane trafficking events delivering vesicles to the cell plate (Smertenko *et al*, 2017a,b). After its insertion in the cortical division site, the cell plate will mature and incorporate new plasma membrane and cell wall. During this process, the phragmoplast expands radially outward around the growing cell plate, transiting from a solid to a ring-like structure. This process requires tight spatio-temporal coordination of cytoskeleton and membrane trafficking (Smertenko *et al*, 2017b). Although details of their cell division machineries differ, cytoskeleton rearrangement and membrane trafficking are necessary and critical for successful cytokinesis in both animals and plants (D'Avino *et al*, 2005; McMichael & Bednarek, 2013).

The lateral expansion of phragmoplasts is regulated via the depolymerization of microtubules in the central part of the phragmoplast and polymerization of tubulins at the periphery (Nishihama & Machida, 2001; Murata *et al*, 2013). Several regulatory players are known to control phragmoplast expansion in plants. In tobacco bright yellow-2 (BY-2) cell cultures, the NPK1-activating kinesin-like proteins (NACKs) directly bind to and activate the mitogen-activated protein kinase kinase kinase (MAPKKK), nucleus- and phragmoplast-localized protein kinase 1 (NPK1; Nishihama *et al*, 2002; Sasabe & Machida, 2012). The activated NPK1 triggers phosphorylation of downstream components of the cascade, such as the MAPKK, NQK1 (Soyano *et al*, 2003), and the MAPK, NRK1 (Soyano *et al*, 2003), constituting the NACK-PQR pathway. NRK1 finally phosphorylates the microtubule-associated protein 65-1 (NtMAP65-1), thereby decreasing its capacity to bundle microtubules, facilitating

<sup>1</sup> Department of Cellular Biochemistry, Institute of Biochemistry and Biotechnology, Martin-Luther-University Halle-Wittenberg, Halle (Saale), Germany

<sup>2</sup> Leibniz Institute of Plant Genetics and Crop Plant Research (IPK) Gatersleben, Seeland, Germany

<sup>3</sup> Biocenter, Martin-Luther-University Halle-Wittenberg, Halle (Saale), Germany

\*Corresponding author. Tel: +49 345 55 24840; Fax: +49 345 55 27013; E-mail: ingo.heilmann@biochemtech.uni-halle.de

turnover and radial expansion of the phragmoplast (Sasabe *et al*, 2006). All counterparts for the tobacco pathway have been identified in *Arabidopsis*, including sequential action of the proteins HINKEL/STUD (homologs of NACK1 and NACK2) activating a MAPK cascade consisting of ANP1-3 (MAPKKs), MKK6/ANQ, and finally MPK4, which can phosphorylate the targets MAP65-1, MAP65-2, and MAP65-3 that are supposed to promote phragmoplast expansion (Strompen *et al*, 2002; Tanaka *et al*, 2004; Beck *et al*, 2010; Takahashi *et al*, 2010; Sasabe *et al*, 2011). In consequence, loss-of-function of *MPK4* results in delayed or abortive transition of mitotic and cytokinetic microtubules and causes heavily bundled microtubules, which ultimately affect the pattern of cell division orientation in the *mpk4-2* mutant (Beck *et al*, 2010, 2011). During cytokinesis, MPK4 and MAP65-3 are both concentrated at the midline of the phragmoplast. MAP65-3 is critical for cytokinesis through bundling anti-parallel microtubules at the midline to establish the phragmoplast microtubule array, while mutation of other members of the MAP65 family does not cause cytokinetic defects (Kosetsu *et al*, 2010; Ho *et al*, 2011). The transition of the phragmoplast from a solid to a ring-like array drives vesicles delivered along phragmoplast microtubules from the center toward the leading edges of the cell plate, resulting in their fusion and leading to the cell plate growing outward (Müller & Jürgens, 2016). Currently, little is known about how membrane trafficking is coordinated in spatio-temporal concert with the lateral expansion of the phragmoplast.

In all eukaryotes, membrane trafficking is controlled by phosphoinositides, a minor class of regulatory phospholipids that are derived from phosphatidylinositol (PtdIns) by phosphorylation of the lipid head group (Munnik & Nielsen, 2011; Gerth *et al*, 2017). Phosphatidylinositol 4-phosphate (PtdIns(4)P) is thought to have functions in the regulation of endomembrane trafficking at the *trans*-Golgi network (TGN; Vermeer *et al*, 2009; Simon *et al*, 2016; Gerth *et al*, 2017). In plant cells, secretion and endocytosis both converge at the TGN (Viotti *et al*, 2010) and make contributions to cell plate formation. A key player of cell plate formation is the cytokinesis-specific syntaxin, KNOLLE, which is by default synthesized only in G2/M phase and endocytosed by clathrin-mediated endocytosis (CME), restricting its distribution to the cell plate during late cytokinesis (Reichardt *et al*, 2007; Boutté *et al*, 2010). As in *Arabidopsis* PtdIns(4)P resides mainly at the plasma membrane, the TGN, and the cell plate (Vermeer *et al*, 2009; Simon *et al*, 2014), we

hypothesized that this lipid may serve a function in cytokinesis and cell plate formation. PtdIns(4)P is produced in *Arabidopsis* by several isoforms of PI4-kinase (PI4K), including PI4K $\alpha$ 1, PI4K $\alpha$ 2, PI4K $\beta$ 1, and PI4K $\beta$ 2 (Mueller-Roeber & Pical, 2002). Even though knockout mutants of *PI4K $\beta$ 1* and *PI4K $\beta$ 2* display a dwarf phenotype (Preuss *et al*, 2006) accompanied by cytokinesis defects (Kang *et al*, 2011), and PtdIns(4)P has been known to reside at the cell plate for some years (Vermeer *et al*, 2009), little is known about how PtdIns(4)P controls cytokinesis in plants, affecting membrane trafficking or cytoskeleton organization, or both.

Here, we show in *Arabidopsis* root cells that PtdIns(4)P formation affects both membrane trafficking and phragmoplast organization during cytokinesis. PI4K $\beta$ 1 furthermore influences the localization of MAP65-3, resulting in altered dynamics of phragmoplast microtubules and defective cytokinesis. Based on similar cytokinetic defects of the *pi4k $\beta$ 1 pi4k $\beta$ 2* and *mpk4* mutants, their genetic interaction, and *in vitro* physical interaction of PI4K $\beta$ 1 and MPK4 proteins, we propose that both PI4K $\beta$  isoforms and MPK4 contribute to the regulation of MAP65-3 and act synergistically to control phragmoplast dynamics during somatic cytokinesis.

## Results

### PI4K $\beta$ 1 is involved in cytokinesis and localizes to the cell plate

To explore the cytokinesis defects of the *Arabidopsis pi4k $\beta$ 1 pi4k $\beta$ 2* double mutant (Preuss *et al*, 2006; Kang *et al*, 2011), we first expressed the coding sequences (CDSs) of *PI4K $\beta$ 1* and *PI4K $\beta$ 2* under their endogenous promoters in the *pi4k $\beta$ 1 pi4k $\beta$ 2* double mutant background. The dwarf phenotype of the double mutant was fully rescued by the ectopic expression of either gene (Fig 1A), indicating that the phenotypes were indeed a result of mutations in *PI4K $\beta$ 1* and *PI4K $\beta$ 2*. Cytokinetic defects were further analyzed by propidium iodide (PI) staining in the single mutants, the double mutant, and the complemented lines. Cell wall stubs or oblique cell walls reported previously for the *pi4k $\beta$ 1 pi4k $\beta$ 2* double mutant (Kang *et al*, 2011) were not found in the complemented lines (Fig 1B and C), indicating the complementation constructs were functional. The complementation also reverted the incidence of oblique cell walls and the reduced meristem size of the *pi4k $\beta$ 1 pi4k $\beta$ 2* double mutant

#### Figure 1. Cytokinetic defects of the *Arabidopsis thaliana pi4k $\beta$ 1 pi4k $\beta$ 2* double mutant.

The *Arabidopsis pi4k $\beta$ 1 pi4k $\beta$ 2* double mutant displays a growth defect and cytokinetic defects.

- The growth phenotype of the *Arabidopsis pi4k $\beta$ 1 pi4k $\beta$ 2* double mutant can be complemented by ectopic expression of *PI4K $\beta$ 1* or *PI4K $\beta$ 2* or by mCherry-tagged *PI4K $\beta$ 1* expressed from a genomic fragment. Plants shown are 1 month old. Scale bar, 10 cm.
- The irregularities in the pattern of root epidermal cell division orientation of the *pi4k $\beta$ 1 pi4k $\beta$ 2* double mutant are also complemented by ectopic expression of *PI4K $\beta$*  variants, as shown by propidium iodide (PI) staining of 5-day-old roots. Arrowhead, oblique cell wall. Insets, magnifications of areas showing cell wall stubs. Scale bars, 50  $\mu$ m.
- Quantifications of cell wall stubs, oblique cell walls and root meristem size (wild type,  $n = 15$  roots; *pi4k $\beta$ 1*,  $n = 15$  roots; *pi4k $\beta$ 2*,  $n = 14$  roots; *pi4k $\beta$ 1 pi4k $\beta$ 2*,  $n = 18$  roots; *pPI4K $\beta$ 1:PI4K $\beta$ 1*,  $n = 14$  roots, *pPI4K $\beta$ 2:PI4K $\beta$ 2*,  $n = 15$  roots). n.d., not detected. Data are mean  $\pm$  SD. Lowercase letters indicate a significant increase of oblique cell walls (Welch ANOVA with Games-Howell *post hoc* test;  $P < 0.0001$ ) or a significant reduction of root meristem size in the *pi4k $\beta$ 1 pi4k $\beta$ 2* double mutant (one-way ANOVA with *post hoc* Tukey HSD;  $P < 0.001$ ).
- Complementation of the *pi4k $\beta$ 1 pi4k $\beta$ 2* phenotype by functional *FLAG-PI4K $\beta$ 1* expressed from the intrinsic *pPI4K $\beta$ 1* or the *pKNOLLE* promoters, as indicated, shown for 1-month-old plants. Scale bar, 10 cm. Complementation with the *pKNOLLE*-driven construct indicates functionality of *PI4K $\beta$ 1* during cell plate formation in G2/M phase.
- PI staining of *pKNOLLE:FLAG-PI4K $\beta$ 1* expressed in the *pi4k $\beta$ 1 pi4k $\beta$ 2* double mutant background indicates rescue of cytokinetic defects. Arrowhead, cell wall stub in the *pi4k $\beta$ 1 pi4k $\beta$ 2* double mutant. Scale bars, 50  $\mu$ m. Further phenotypic aspects of the *pKNOLLE:FLAG-PI4K $\beta$ 1*-complemented double mutants can be seen in Appendix Fig S1.

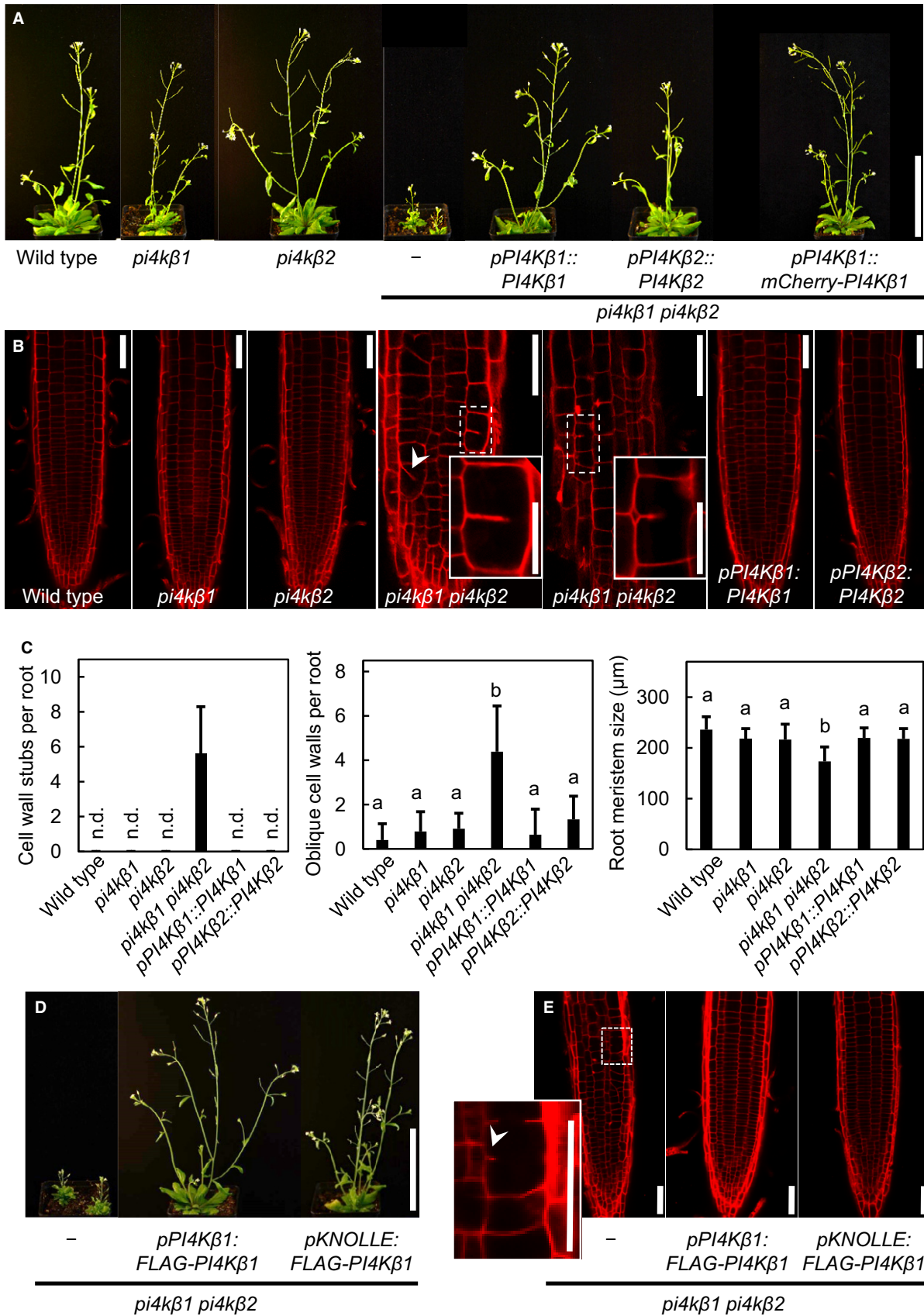


Figure 1.

(Fig 1C). Further experiments were initiated to determine the subcellular localization of PI4K $\beta$ 1 in cytokinetic root cells of *Arabidopsis*. To our knowledge, no functional fluorescence-tagged PI4K $\beta$ 1 or PI4K $\beta$ 2 has been reported, so the *in vivo* localization of PI4K $\beta$  isoforms in *Arabidopsis* has remained unclear. Therefore, we developed functional complementation constructs, either fusing the CDS of an N-terminal mCherry tag upstream of an 11-kb genomic fragment of the *PI4K $\beta$ 1* gene including introns, 5' UTR, 3' UTR, and parts of sequences of the upstream and downstream neighboring genes or fusing an N-terminal FLAG tag for immunodetection. We focused on PI4K $\beta$ 1, as it has 83% identity to PI4K $\beta$ 2 and the enzymes are functionally redundant (Preuss *et al.*, 2006). Both the mCherry-tagged PI4K $\beta$ 1 and the FLAG-tagged PI4K $\beta$ 1 complemented the phenotype of the *pi4k $\beta$ 1 pi4k $\beta$ 2* double mutant (Fig 1A, D and E) and were thus found functional for further analyses. To further test the contribution of PI4K $\beta$ 1 to the control of cytokinesis, a functional *FLAG-PI4K $\beta$ 1* construct was expressed in *pi4k $\beta$ 1 pi4k $\beta$ 2* double mutants under the control of KNOLLE cis-regulatory elements (*pKNOLLE:FLAG-PI4K $\beta$ 1*), aiming to confine *FLAG-PI4K $\beta$ 1* expression to cells in the G2/M phase of the cell cycle (Muller *et al.*, 2003; Fig 1D and E). The *pKNOLLE:FLAG-PI4K $\beta$ 1* rescued the growth and cytokinetic/cell division orientation defects of the *pi4k $\beta$ 1 pi4k $\beta$ 2* double mutant (Fig 1E and Appendix Fig S1A), but not previously reported root hair defects (Preuss *et al.*, 2006; Appendix Fig S1B), suggesting involvement of PI4K $\beta$ s in cytokinesis as well as in other cellular processes. We tried to investigate PI4K $\beta$ 1 localization in *pKNOLLE:FLAG-PI4K $\beta$ 1* lines and *pPI4K $\beta$ 1:FLAG-PI4K $\beta$ 1* lines by immunostaining. However, the FLAG-PI4K $\beta$ 1 fusion was not detected by staining or in Western blots even when using different anti-FLAG antibodies, so the persistence of the expressed protein beyond G2/M phase cannot be judged. Expression of FLAG-PI4K $\beta$ 1 was verified in a membrane fraction of the *pPI4K $\beta$ 1:FLAG-PI4K $\beta$ 1* line (Appendix Fig S2A and B) using a custom anti-PI4K $\beta$ 1 antibody against the C-terminal fifteen amino acids of PI4K $\beta$ 1 (TRQYDYYQRVNLGIL) re-raised as reported previously (Preuss *et al.*, 2006). The specificity of this antibody was verified by analyzing crude extracts from wild-type *Arabidopsis*, the *pi4k $\beta$ 1* single mutant, or the *pi4k $\beta$ 1 pi4k $\beta$ 2* double mutant. The antibody recognized a band at 130 kDa corresponding to the size of the PI4K $\beta$ 1 or PI4K $\beta$ 2 proteins in wild-type protein extracts, but not in *pi4k $\beta$ 1* or *pi4k $\beta$ 1 pi4k $\beta$ 2* mutants (Appendix Fig S2A), indicating the antibody specifically recognized PI4K $\beta$ 1. While the antibody detected PI4K $\beta$ 1 on immunoblots, PI4K $\beta$ 1 was not detected by immunofluorescence in wild-type samples nor in the partially complemented double mutants expressing PI4K $\beta$ 1 from the *pKNOLLE* promoter (Appendix Fig S2C). Instead, the antibody gave rise to unspecific signals in interphase cells even of root cells of *pi4k $\beta$ 1 pi4k $\beta$ 2* double mutants (Appendix Fig S2C), so the persistence of the PI4K $\beta$ 1

protein expressed from the *pKNOLLE* promoter could not be judged. As a kinase-dead variant of PI4K $\beta$ 1 was previously unable to rescue the phenotypes of the *pi4k $\beta$ 1 pi4k $\beta$ 2* double mutant (Antignani *et al.*, 2015), we concluded from the combined complementation data that one function of PI4K $\beta$ 1 in *Arabidopsis* is the formation of PtdIns(4)P during somatic cytokinesis, but that PI4K $\beta$ 1 also has regulatory functions in interphase cells.

The fluorescence of the functional mCherry-PI4K $\beta$ 1 fusion expressed in the *pi4k $\beta$ 1 pi4k $\beta$ 2* double mutant decorated the cell plate of cytokinetic root cells *in vivo* (Fig 2A). As *in vivo* fluorescence was weak, subsequent whole-mount immunostaining was performed and clearly showed mCherry-PI4K $\beta$ 1 residing in cytokinetic cells at the cell plate (Fig 2B) from early to late cytokinesis and concentrated at the leading edges of the cell plate (Fig 2B [I], [II]). No signal was observed using wild-type plants as a negative control (Appendix Fig S3), indicating the mCherry detection was specific. Under its intrinsic promoter, the mCherry-PI4K $\beta$ 1 fusion was also expressed in prophase and metaphase, and the marker fluorescence showed punctate and diffuse localization patterns (Fig 2B), suggesting PI4K $\beta$ 1 also has functions outside cytokinesis. Therefore, the localization of mCherry-PI4K $\beta$ 1 was further evaluated by immunofluorescence relative to the TGN marker, ARF1 (Boutté *et al.*, 2010), and the fluorescence patterns largely co-localized (Fig 2C), consistent with previously reported TGN localization of PI4K $\beta$ 1 (Preuss *et al.*, 2006; Kang *et al.*, 2011).

As in cytokinetic cells PI4K $\beta$ 1 was localized to leading edges of cell plates (Fig 2B and C), the main area where incoming vesicles fuse to contribute to cell plate growth (Seguí-Simarro *et al.*, 2004), one would expect that fusion of vesicles at the cell plate might be altered in the *pi4k $\beta$ 1 pi4k $\beta$ 2* mutant. As expected, using transmission electron microscopy (TEM) we did find numerous unfused vesicles in cytokinetic root cells of the *pi4k $\beta$ 1 pi4k $\beta$ 2* mutant and the cell plate was not well defined (Fig 3A and B; black arrowheads), in contrast to coordinated fusion of vesicles at a clearly defined nascent cell plate in wild-type cells (Fig 3A). We further observed that cell wall stubs were surrounded by two types of unfused vesicles (Fig 3C; black and white arrowheads, respectively). In addition, we also observed totally blocked cytokinesis, i.e., no cross-walls at all (Fig 3D). Overall, the TEM analysis confirms that *pi4k $\beta$ 1 pi4k $\beta$ 2* mutants display previously reported membrane trafficking defects (Preuss *et al.*, 2006; Kang *et al.*, 2011), which we further explored.

### PtdIns(4)P production and clathrin-mediated endocytosis at the cell plate are impaired in the *pi4k $\beta$ 1 pi4k $\beta$ 2* double mutant

The association of a biosensor for PtdIns(4)P, 2xmCherry<sub>FAPP1-PH</sub> (Vermeer *et al.*, 2009; Simon *et al.*, 2014), with the cell plate

**Figure 2. PI4K $\beta$ 1 localization at the cell plate and the TGN during cytokinesis in *Arabidopsis* root cells.**

- A *In vivo* localization of mCherry-PI4K $\beta$ 1 expressed from the *pPI4K $\beta$ 1* promoter in root tips of 5-day-old complemented *pi4k $\beta$ 1 pi4k $\beta$ 2* plants. The mCherry-PI4K $\beta$ 1 distribution was imaged using a Zeiss LSM880 in Airyscan Virtual Pinhole (VP) mode with the pinhole set to 2. Arrowheads, nascent cell plates decorated by mCherry-PI4K $\beta$ 1. Scale bar, 20  $\mu$ m.
- B Whole-mount immunostaining of 5-day-old seedlings expressing mCherry-PI4K $\beta$ 1 in the *pi4k $\beta$ 1 pi4k $\beta$ 2* double mutant background using anti-tubulin (red) and anti-mCherry (green) antibodies, and DAPI (blue). (I), (II), magnifications of regions marked in b, representing early and late cytokinetic stages. Scale bars, 20  $\mu$ m.
- C Relative localization of mCherry-PI4K $\beta$ 1 and the TGN marker, ARF1, during cytokinesis. Four-day-old seedlings were immunostained with anti-mCherry (green) and anti-ARF1 (red) antibodies. Scale bars are 10  $\mu$ m. Further controls for the use of the anti-mCherry antibodies can be seen in Appendix Fig S3.

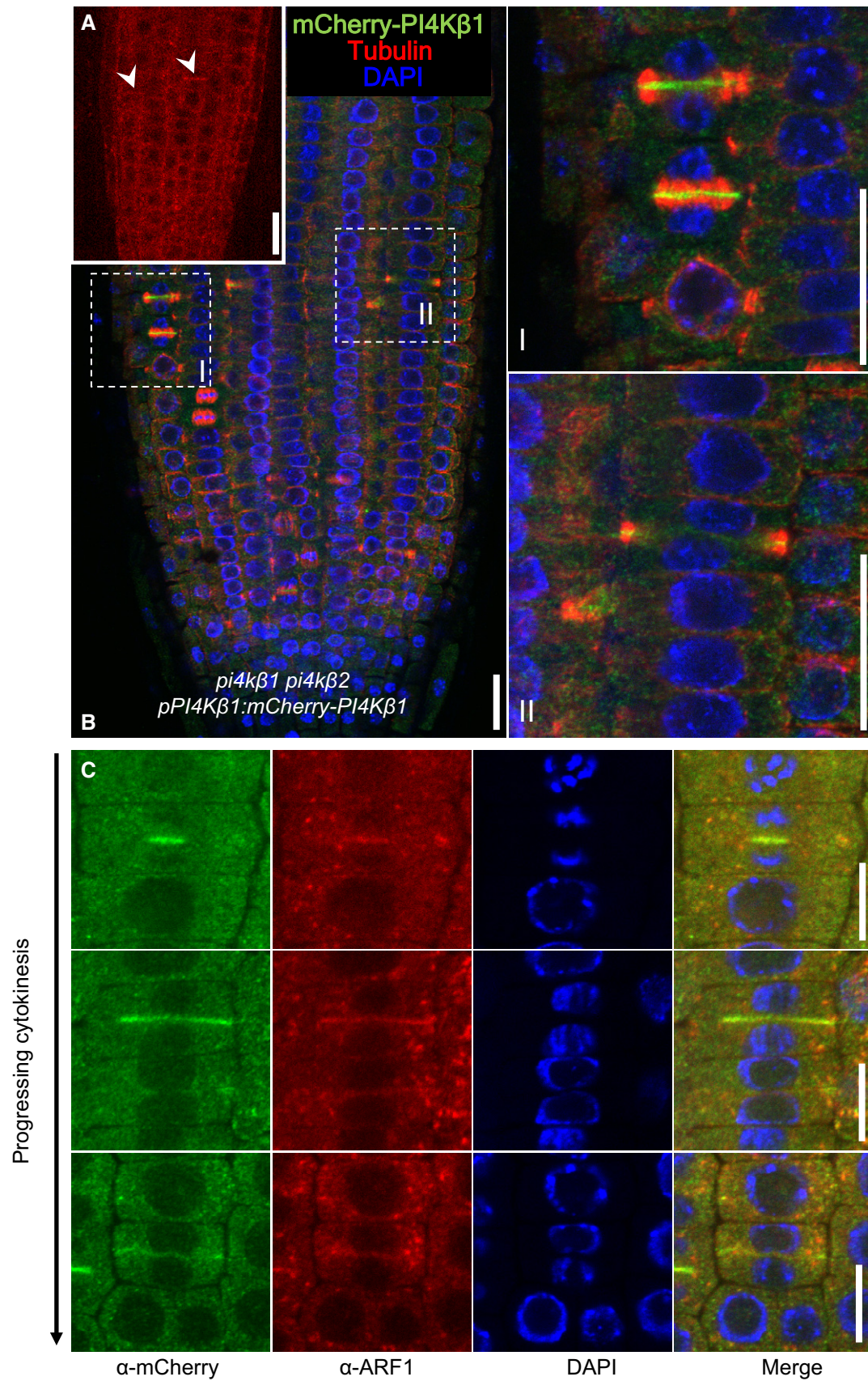
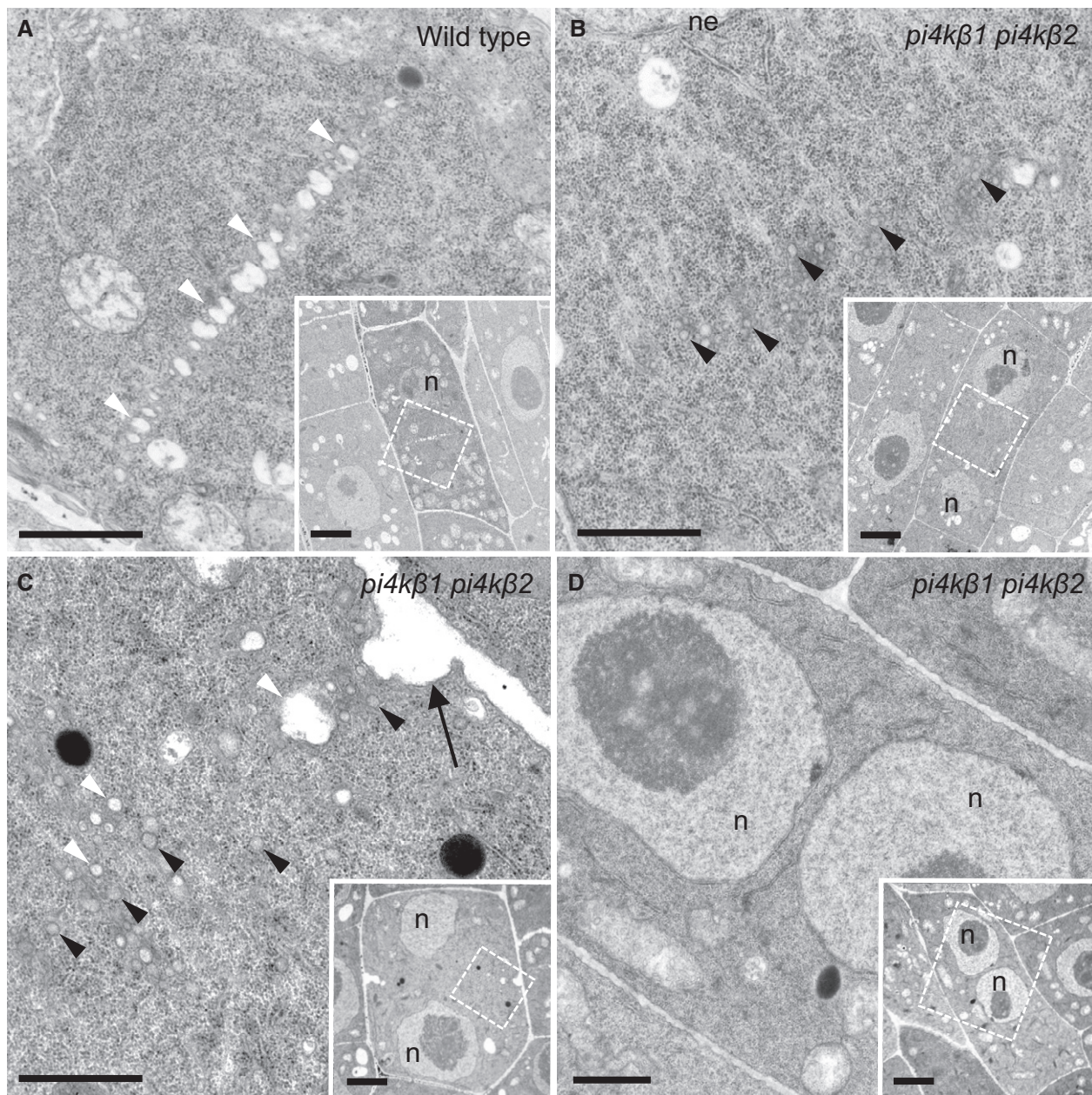


Figure 2.



**Figure 3. Ultrastructure of cytokinetic defects in root tips of *Arabidopsis pi4kβ1 pi4kβ2* double mutants.**

A, B The ultrastructure of cytokinetic defects was analyzed by transmission electron microscopy of 5-day-old root tip meristems. Images shown are from three roots (wild type) and seven roots (*pi4kβ1 pi4kβ2* double mutant). In wild-type controls (A), vesicles fused at the cell division plane to give rise to the tubular network (TN) of a nascent cell plate. White arrowheads, fused vesicles at the division plane.  $n = 8$  cells. In the *pi4kβ1 pi4kβ2* double mutant (B), vesicles were delivered to the cell division plane at a similar stage as wild type but did not fuse. The nuclei of both wild-type and double mutant cells were at telophase or interphase, as judged by the presence of decondensed chromatin and a nuclear envelope. At this stage, failed cell plate formation was never seen in wild type (A). Black arrowheads, unfused vesicles.  $n = 6$  cells.

C Unfused vesicles clustered around a cell wall stub (arrow). White arrowheads, light vesicles; black arrowheads, dark vesicles; black arrow, cell wall stub.  $n = 8$  cells.

D No cross-wall was seen in this cell with two nuclei.  $n = 6$  cells.

Data information: Insets, overviews; dashed boxes, areas of magnification. n, nucleus; ne, nuclear envelope. Scale bars in magnified figures, 2  $\mu\text{m}$ ; in insets, 1  $\mu\text{m}$ .

appeared reduced in cytokinetic cells of the *pi4kβ1 pi4kβ2* double mutant compared to wild-type controls at equivalent stages at the end of cytokinesis (Fig 4A), suggesting a PtdIns(4)P-dependent defect. It should be noted that in cytokinetic cells of the *pi4kβ1*

*pi4kβ2* double mutant, the cell plate appeared slightly diffuse, possibly interfering with precise quantification of reporter intensities. As furthermore the *in vivo* use of fluorescent reporters for phosphoinositides has its caveats (Balla *et al*, 2000; Varnai & Balla, 2008;

**Figure 4. Delayed recruitment of clathrin to the cell plate in the *Arabidopsis pi4kβ1 pi4kβ2* double mutant.**

The effects of reduced association of PtdIns(4)P with the cell plate on the recruitment of CLC2-GFP were analyzed in root meristem cells of 5-day-old plants.

- A** Top: Cell plate-associated fluorescence of the PtdIns(4)P reporter, 2xmCherry<sub>FAPP1-PH</sub>, was monitored at the end of cytokinesis in 5-day-old wild-type controls or *pi4kβ1 pi4kβ2* double mutants, as indicated. Scale bars, 10 μm. Bottom: The intensity of 2xmCherry<sub>FAPP1-PH</sub> signals was quantified at the end of cytokinesis at the cell plate (left plot) and at the TGN (right plot). Signal intensities at the cell plate were recorded along the dashed lines indicated in the images and normalized to intensities at the apical plasma membrane (wild type,  $n = 37$  cells, 24 roots; *pi4kβ1 pi4kβ2*,  $n = 55$  cells, 41 roots). TGN intensities were recorded using the Airyscan VP mode, and the mean TGN intensity was normalized to mean apical and basal plasma membrane intensity (wild type,  $n = 30$  cells, 22 roots; *pi4kβ1 pi4kβ2*,  $n = 37$  cells, 31 roots). \*\*\*, significant differences ( $P < 0.0001$ ) according to two-tailed Mann–Whitney  $U$ -tests.
- B, C** Image series from live-cell time-lapse analysis of CLC2-GFP at the cell plate in roots of wild-type or *pi4kβ1 pi4kβ2* seedlings costained with FM 4-64, as indicated. Arrowheads, appearance of CLC2-GFP at the cell plate. Times are given relative to the instance when the cell plate contacted the peripheral plasma membrane, defined as  $t_0$ . Scale bars, 10 μm. Images are from median focal planes chosen from time-lapse series recorded as 3D stacks. 3D projections of the  $t_0$  images for wild type and double mutant and results for CLC2-recruitment based on immunostaining can be seen in Appendix Fig S6.
- D** Left, quantification of the time of CLC2-GFP appearance at the cell plate in wild type (B) or the *pi4kβ1 pi4kβ2* double mutant (C) (wild type,  $n = 10$  cells, 7 roots; *pi4kβ1 pi4kβ2*,  $n = 24$  cells, 19 roots). Right, quantification of CLC2-GFP at the TGN in interphase cells. Five-day-old roots expressing CLC2-GFP were subjected to immunostaining, and the mean TGN intensity was normalized to plasma membrane intensity (wild type,  $n = 14$  cells, 2 roots; *pi4kβ1 pi4kβ2*,  $n = 15$  cells, 2 roots). \*\*\*, a significant difference ( $P < 0.0001$ ) according to a two-tailed Student's  $t$ -test.

Heilmann, 2016; Gerth *et al*, 2017), and specifically the FAPP1-PH module may also bind to the TGN-associated ARF1 protein (Godi *et al*, 2004; He *et al*, 2011; Liu *et al*, 2014), we confirmed by immunofluorescence that the distribution of ARF1 was not altered in the *pi4kβ1 pi4kβ2* double mutant (Appendix Fig S4). With these reservations, a decreased abundance of the 2xmCherry<sub>FAPP1-PH</sub> reporter was observed at the cell plate (Fig 4A). This pattern is particularly interesting, because the fluorescence intensity of the reporter at the plasma membrane did not considerably change, suggesting that PI4Kβ1 and PI4Kβ2 might not contribute substantially to the production of PtdIns(4)P at the plasma membrane. This notion is also supported by biochemical analyses of lipid levels in *Arabidopsis* root tissue, which consists mostly of interphase cells. These analyses did not indicate a significant difference in PtdIns(4)P abundance between wild type, *pi4kβ1* and *pi4kβ2* single mutants, the double mutant, or complemented lines ectopically expressing either *PI4Kβ1* or *PI4Kβ2* from their respective intrinsic promoters in the *pi4kβ1 pi4kβ2* double mutant background (Appendix Fig S5). At the cell plate of *pi4kβ1 pi4kβ2* double mutant cells, the 2xmCherry<sub>FAPP1-PH</sub> signal was reduced but not fully abolished (Fig 4A, left plot), consistent with a localized and/or limited contribution of PI4Kβ isoforms to PtdIns(4)P production even in this specialized compartment. Interestingly, the association of the 2xmCherry<sub>FAPP1-PH</sub> with the trans-Golgi-network (TGN) was also reduced in the *pi4kβ1 pi4kβ2* double mutant (Fig 4A, right plot). Given that in yeast the knockdown of the PI4K, *Pik1p*, inhibits the recruitment of clathrin to the Golgi (Gloor *et al*, 2010) and that plant phosphoinositides have previously been linked to clathrin dynamics (Ischebeck *et al*, 2013; Gerth *et al*, 2017), we hypothesized that clathrin dynamics may be affected in the *Arabidopsis pi4kβ1 pi4kβ2* double mutant. While defective secretion has previously been reported for the *pi4kβ1 pi4kβ2* mutant (Preuss *et al*, 2006; Kang *et al*, 2011), we therefore investigated whether additionally endocytosis and/or clathrin recruitment might be impaired. To test this hypothesis, a clathrin light chain 2 (CLC2)-GFP marker (Konopka *et al*, 2008) was introgressed into the *pi4kβ1 pi4kβ2* double mutant and its association with the cell plate was analyzed by live-cell time-lapse imaging in root cells undergoing cytokinesis (Fig 4B–D, Movies EV1 and EV2). The timing of fluorescence patterns for wild type and mutant is reported relative to the time point when the cell plate attaches to the peripheral plasma membrane, here defined as  $t_0$  (Fig 4B and C). In cytokinetic cells of wild-type controls, the CLC2-GFP marker was recruited at  $\sim 6.6 \pm 5.3$  min relative to  $t_0$

(Fig 4B and D). In contrast, in cytokinetic cells of the *pi4kβ1 pi4kβ2* double mutant the recruitment of CLC2-GFP to the cell plate was significantly delayed and only occurred  $\sim 11.6 \pm 12.1$  min after the cell plate attached to the plasma membrane (Fig 4C and D). Immunostaining performed during advanced cytokinetic stages showed an association of CLC2-GFP with the cell plate for 98.1% of analyzed cells ( $n = 53$ ) of wild-type controls, but only for 27.0% of analyzed cells ( $n = 126$ ) of the *pi4kβ1 pi4kβ2* double mutant, confirming reduced association of CLC2-GFP with the cell plate in the mutant (Appendix Fig S6). The reduced or delayed recruitment of CLC2-GFP to the cell plate of cytokinetic cells was accompanied by an enhanced intensity of the CLC2-GFP marker at the TGN (Fig 4D, right plot), as observed by immunofluorescence experiments, suggesting that the lesion in the *PI4Kβ1* and *PI4Kβ2* genes influenced processes also at the TGN, with possible regulatory consequences in or apart from cytokinesis. As effects of *PI4Kβ1* or *PI4Kβ2* on endocytosis might not be restricted to cytokinetic cells, we also tested clathrin dynamics in interphase cells of wild type and *pi4kβ1 pi4kβ2* double mutants by spinning disk microscopy (Appendix Fig S7) and found a significantly increased lifetime of  $24 \pm 8$  s for CLC2-GFP foci at the plasma membrane in the *pi4kβ1 pi4kβ2* double mutant vs.  $19 \pm 4$  s in wild-type controls (Appendix Fig S7C;  $P < 0.0001$ ;  $n = 134$  events for wild type;  $n = 130$  events for *pi4kβ1 pi4kβ2*). Overall, the dynamics of CLC2-GFP were thus found to be altered in both cytokinetic and interphase cells of the *pi4kβ1 pi4kβ2* double mutant. Based on this notion, we next tested for defects in clathrin-mediated endocytosis (CME). During cytokinesis, CME is involved in cell plate expansion and maturation (Ito *et al*, 2012). A key factor for cell plate formation during cytokinesis is the syntaxin KNOLLE, which requires CME for correct trafficking (Boutté *et al*, 2010). Based on immunostaining of cytokinetic cells, KNOLLE displayed increased association with the plasma membrane in the *pi4kβ1 pi4kβ2* double mutant (Fig 5A and B), consistent with a defect in CME during cytokinesis (Boutté *et al*, 2010). Moreover, we observed significantly enhanced signals for KNOLLE (Fig 5C and D) and the auxin transporter PIN-FORMED2 (PIN2)-GFP (Fig 5E and F) at the cell plate of cytokinetic cells of *pi4kβ1 pi4kβ2* double mutants, indicating defects either in CME from or in vesicle fusion with the cell plate. An impairment of CME in the *pi4kβ1 pi4kβ2* double mutant was not restricted to cytokinesis, as the formation of BFA bodies decorated by PIN2-GFP (Fig 5G and H) and the uptake of the membrane dye, FM 4-64, from the plasma membrane (Fig 5I and J) were also significantly

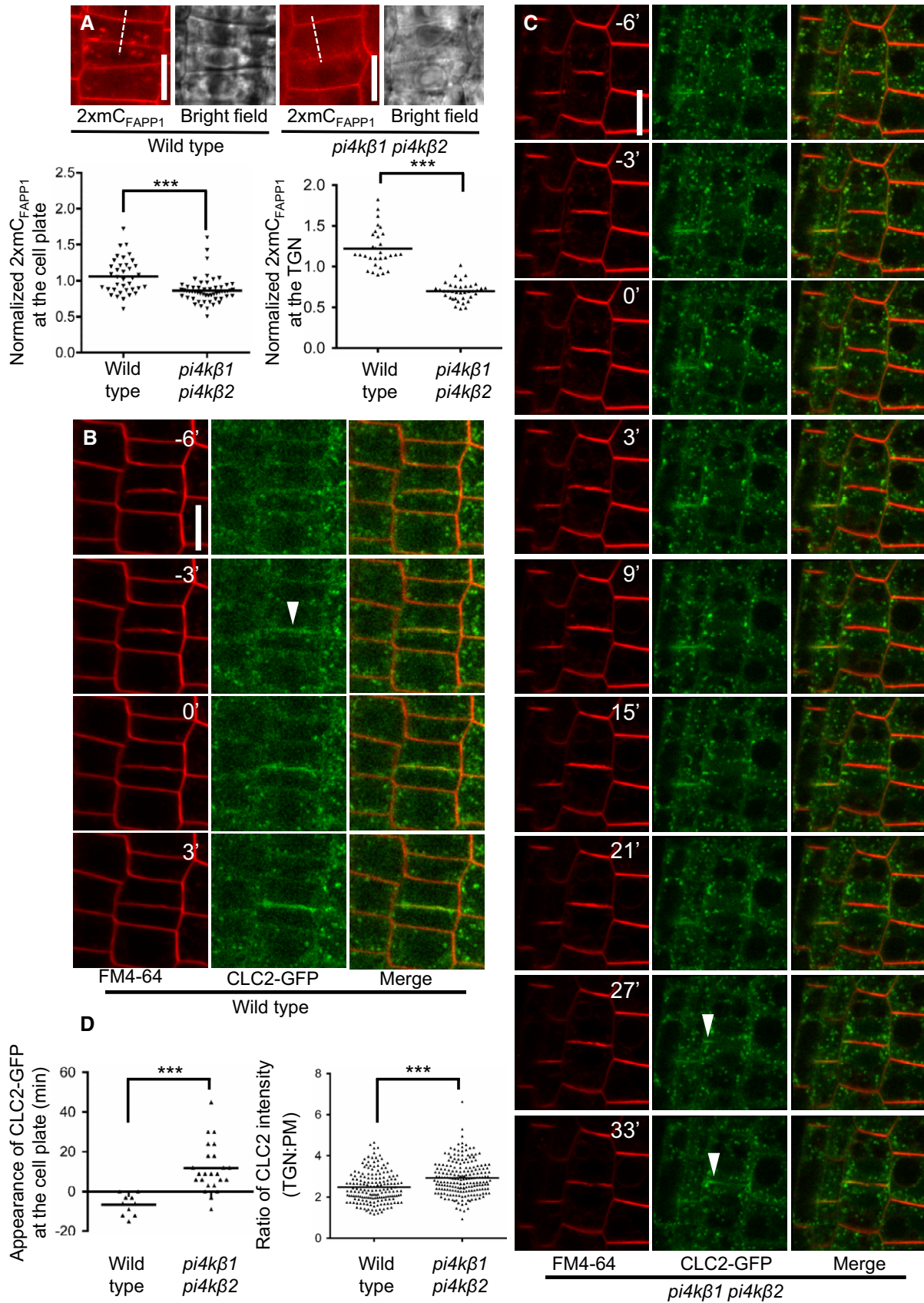


Figure 4.



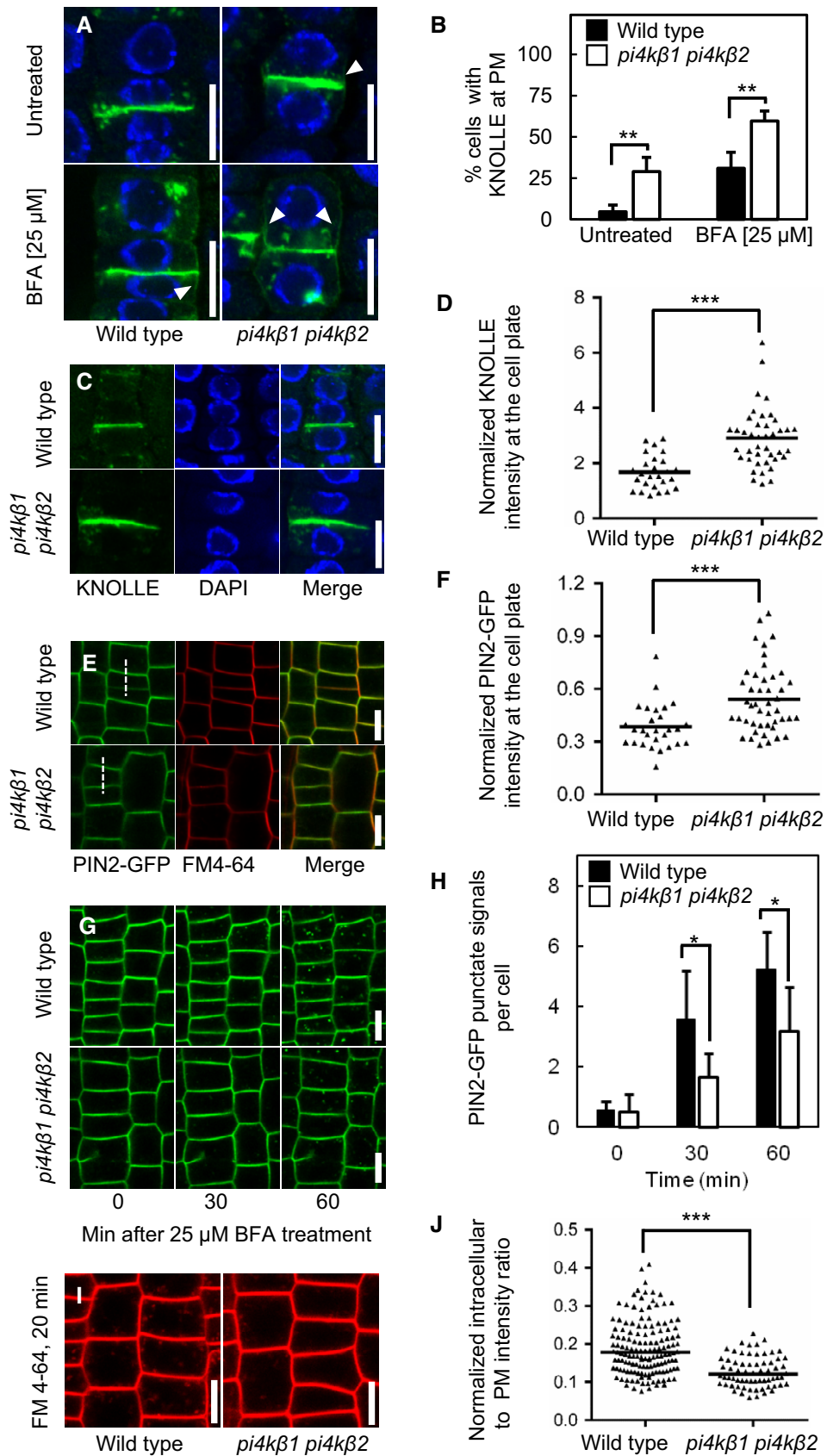


Figure 5.

**Figure 5. Impaired endocytosis in the *Arabidopsis pi4kβ1 pi4kβ2* double mutant.**

Experiments were performed to address possible effects of the *pi4kβ1 pi4kβ2* double mutant on endocytosis of markers relevant for cell plate formation. Panels (A–F) display data obtained using cytokinetic cells; panels (G–J) display data from the analysis of interphase cells.

- A Five-day-old seedlings were immunostained with anti-KNOLLE (green) and counterstained with DAPI (blue). In the *pi4kβ1 pi4kβ2* double mutant, diffusion of KNOLLE occurred at the plasma membrane (arrowheads). Scale bars, 10  $\mu$ m.
- B Quantitative analysis of lateral diffusion of KNOLLE at the plasma membrane (PM) from (A). Data are mean  $\pm$  SD from four independent experiments. \*\*, a significant difference ( $P < 0.01$ ) according to a two-tailed Student's *t*-test (untreated wild type,  $n = 97$  cells, 25 roots; untreated *pi4kβ1 pi4kβ2*,  $n = 142$  cells, 44 roots; BFA-treated wild type,  $n = 126$  cells, 28 roots; BFA-treated *pi4kβ1 pi4kβ2*,  $n = 183$  cells, 43 roots).
- C Enhanced accumulation of KNOLLE at the cell plate at the end of cytokinesis in the *pi4kβ1 pi4kβ2* double mutant. Five-day-old seedlings were immunostained with anti-KNOLLE antibodies (green) and counterstained with DAPI (blue). Scale bars, 10  $\mu$ m.
- D Quantification of KNOLLE intensity at the cell plate from (C), normalized to the signal intensity of intracellular compartments. \*\*\*, a significant difference ( $P < 0.0001$ ) according to a two-tailed Mann–Whitney *U*-test (wild type,  $n = 26$  cells, 20 roots; *pi4kβ1 pi4kβ2*,  $n = 41$  cells, 37 roots).
- E Enhanced accumulation of PIN2-GFP at the cell plate at the end of cytokinesis in the *pi4kβ1 pi4kβ2* double mutant. Five-day-old seedlings were stained with 2  $\mu$ M FM 4-64 for 3 min at room temperature. Scale bars, 10  $\mu$ m.
- F Quantification of PIN2-GFP signal at the cell plate from (E), normalized to the intensity at the apical plasma membrane intensity, as indicated by the dashed lines. \*\*\*, a significant difference ( $P < 0.001$ ) according to a two-tailed Mann–Whitney *U*-test (wild type,  $n = 28$  cells, 16 roots; *pi4kβ1 pi4kβ2*,  $n = 45$  cells, 26 roots).
- G Internalization of PIN2-GFP was tracked over time in live roots pretreated with 50  $\mu$ M CHX for 30 min, then washed, and incubated with 50  $\mu$ M CHX and 25  $\mu$ M BFA. Scale bars, 10  $\mu$ m.
- H Quantification of punctate signals from (G) induced by BFA in wild type and *pi4kβ1 pi4kβ2* double mutants. Data are mean  $\pm$  SD. \*, a significant difference ( $P < 0.05$ ) according to a two-tailed Student's *t*-test (wild type,  $n = 116$  cells, 6 roots; *pi4kβ1 pi4kβ2*,  $n = 110$  cells, 7 roots).
- I Delayed internalization of FM 4-64 from the plasma membrane in the *pi4kβ1 pi4kβ2* double mutant. Four-day-old seedlings were pulsed with 2  $\mu$ M FM 4-64 for 3 min on ice, and then, fluorescence was recorded for 20 min. Scale bars, 10  $\mu$ m.
- J Quantification of intracellular FM 4-64 signal from (I), normalized to apical and basal plasma membrane intensities. \*\*\*, a significant difference ( $P < 0.0001$ ) according to a two-tailed Mann–Whitney *U*-test (wild type,  $n = 116$  cells, 6 roots; *pi4kβ1 pi4kβ2*,  $n = 66$  cells, 9 roots).

reduced in interphase cells of the *pi4kβ1 pi4kβ2* double mutant. Overall, our data indicate a function of PI4Kβ1 and PI4Kβ2 in endocytosis of both cytokinetic and interphase cells. During cytokinesis, PI4Kβ1 or PI4Kβ2 is likely required at the cell plate for correct trafficking of key markers of cell plate formation, such as KNOLLE and PIN2. It is possible that a role of PI4Kβ1 and PI4Kβ2 in the correct trafficking of these and other markers is in maintaining the delicate balance of secretion and retrieval of vesicles upon delivery of cargoes to the cell plate, as well as—possibly—the removal of excess deposited material from the cell plate.

**The *Arabidopsis pi4kβ1 pi4kβ2* double mutant displays multinucleated cells and aberrant phragmoplasts**

While impaired membrane trafficking might account for part of the cytokinetic defects of the *pi4kβ1 pi4kβ2* double mutant, we observed additional aspects of the *pi4kβ1 pi4kβ2* double mutant phenotype that were not previously reported (Fig 6). In particular, an enhanced incidence of multinucleated cells and of cells with several persisting phragmoplasts was found in root cells of the *pi4kβ1 pi4kβ2* double mutant (Fig 6A–C). These elements were not observed in wild-type controls, indicating that further key aspects of cell division were impaired in the mutant. In cytokinetic wild-type cells, immunostaining showed the phragmoplasts associated with

the leading edges of the cell plate during late cytokinesis (Fig 6B), consistent with a model where central phragmoplast microtubules depolymerize and peripheral microtubules polymerize (Murata *et al*, 2013). In contrast, in cytokinetic cells of the *pi4kβ1 pi4kβ2* double mutant the central areas of phragmoplasts were still solid even in late cytokinesis (Fig 6B), indicating that microtubules were ectopically stabilized. As phragmoplasts undergo dynamic transitions from initiation to solid, ring, and discontinuous stages during cytokinesis and finally disband to form cortical microtubules (Smertenko *et al*, 2017a), the defects in phragmoplast dynamics were assessed in more detail by time-lapse imaging. To achieve this, we introgressed the microtubule marker mCherry-TUA5 into the *pi4kβ1 pi4kβ2* double mutant and performed live-cell time-lapse imaging on cytokinetic cells of wild-type controls and double mutants (Fig 7, Movies EV3 and EV4). In cytokinetic cells of wild-type controls, phragmoplasts persisted over a period of  $\sim 31.75 \pm 12.00$  min and underwent all cytokinetic stages (Smertenko *et al*, 2017a; Fig 7A) before disbanding to form cortical microtubule arrays (Fig 7A, Movie EV3). By contrast, in cytokinetic cells of the *pi4kβ1 pi4kβ2* double mutant, phragmoplasts persisted for a significantly longer time of  $\sim 72.95 \pm 48.88$  min (Fig 7B), appeared disordered, and did not display recognizable cytokinetic stages (Fig 7A, Movie EV4). Even though in cytokinetic cells of the double mutant microtubules were stabilized in the central zone of the cell plate and did not

**Figure 6. Multinucleated cells and aberrant phragmoplasts in root cells of the *Arabidopsis pi4kβ1 pi4kβ2* double mutant.**

Further aspects of the *pi4kβ1 pi4kβ2* double mutant phenotype were recorded.

- A Immunostaining of meristem cells of 5-day-old plants using anti-tubulin (green) counterstained with DAPI (false color red). Asterisks, multiple nuclei in one cell; arrowheads, multiple phragmoplasts in one cell. Dashed lines indicate the outlines of exemplary multinucleated cells. Scale bars, 10  $\mu$ m.
- B Whole-mount immunostaining of root tips of 5-day-old seedlings. Green, anti-KNOLLE; red, anti-tubulin; blue, DAPI. (I), (II), magnifications of areas highlighted in dashed boxes. Arrowheads, solid phragmoplasts with thicker cell plates. Scale bars, 20  $\mu$ m.
- C Quantification of the incidences of multinucleated cells, multiple phragmoplasts, and solid phragmoplasts during late cytokinesis (multinucleated cells: wild type,  $n = 316$  cells, 29 roots; *pi4kβ1 pi4kβ2*,  $n = 673$  cells, 44 roots; multiple phragmoplasts: wild type,  $n = 64$  cells, 29 roots; *pi4kβ1 pi4kβ2*,  $n = 188$  cells, 44 roots; solid phragmoplast in late cytokinesis: wild type,  $n = 41$  cells, 29 roots; *pi4kβ1 pi4kβ2*,  $n = 89$  cells, 44 roots). Data are mean  $\pm$  SD from three independent experiments. n.d., not detected.

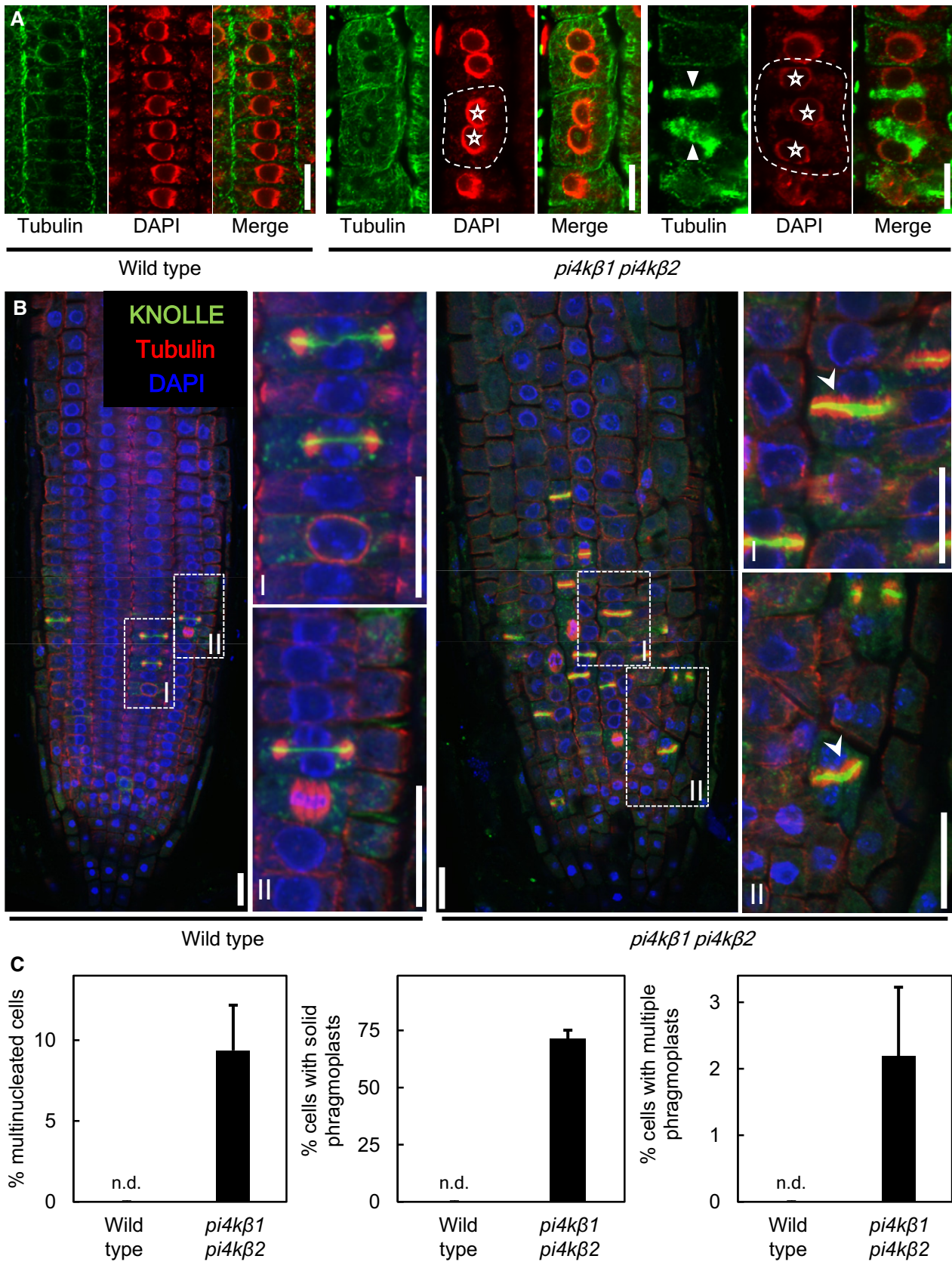


Figure 6.

follow the leading edge, phragmoplast transition nonetheless progressed continuously to finally disband and form cortical microtubule arrays (Fig 7A). However, substantial proportions of microtubules lingered in an irregular pattern at the cell plate even after parts had already moved to a perinuclear or cortical orientation. It should be noted that cytokinetic defects in the *pi4kβ1 pi4kβ2* double mutant appeared to varying degrees, with cell plates ranging from close-to-normal to absent. For better comparison with the wild type, Fig 7A depicts a time-lapse series of a mildly impaired cell plate, where the time between initiation and transition to cortical microtubules was roughly the same as in wild-type controls. The data from our combined time-lapse analyses on cytokinetic cells indicate a significant stabilization of phragmoplast microtubules in cytokinetic cells of the *pi4kβ1 pi4kβ2* double mutant during cytokinesis (Fig 7B) ( $P < 0.001$ ;  $n = 12$  cells for wild type;  $n = 21$  cells for *pi4kβ1 pi4kβ2*). The stabilization of phragmoplast microtubules in the central zone of the growing cell plate of cytokinetic cells of the *pi4kβ1 pi4kβ2* double mutant is further supported by the observation of an extended period of disk-like phragmoplasts (Fig 7C) and from the extended duration between phragmoplast initiation and disbanding (Fig 7D) observed in these cells. Because of robust microtubule bundles in the phragmoplast, it is often difficult to measure the dynamics of phragmoplast microtubules. For interphase cells of the *pi4kβ1 pi4kβ2* double mutant, we determined dynamic parameters for cortical microtubules from cells of the root elongation zone by spinning disk microscopy (Appendix Fig S8). Most parameters of microtubule dynamics were globally unchanged in interphase cells of the *pi4kβ1 pi4kβ2* double mutant, including density, bundling, and the rates of polymerization, indicating there were no gross defects in microtubule arrays. However, the microtubular rate of shrinkage in interphase cells of the *pi4kβ1 pi4kβ2* double mutant was at  $8.3 \pm 5.3 \mu\text{m min}^{-1}$  significantly lower than in interphase cells of wild-type controls at  $11.1 \pm 7.1 \mu\text{m min}^{-1}$  ( $P < 0.05$ ;  $n = 68$ , 6 roots for wild type;  $n = 53$ , 5 roots for *pi4kβ1 pi4kβ2*; Appendix Fig S8). While the information from the interphase cells does not pertain to phragmoplast microtubules in cytokinetic cells, the data are consistent with stabilized phragmoplast arrays observed in cytokinetic cells of the *pi4kβ1 pi4kβ2* double mutant, possibly in consequence of reduced shrinkage rates.

### MAP65-3 mislocalizes in *pi4kβ1 pi4kβ2* double mutants

A key player controlling microtubule stability and phragmoplast dynamics is the microtubule-associated protein 65-3 (MAP65-3), also known as PLEIADE (PLE; Müller *et al.*, 2004). Loss-of-function of MAP65-3 results in severe cytokinetic defects (Müller *et al.*,

2004), whereas mutations in its isoforms MAP65-1 and/or MAP65-2 do not influence cytokinesis (Lucas & Shaw, 2012). In cytokinetic cells, MAP65-3 is concentrated at the midline of the phragmoplast to cross-link anti-parallel microtubules during cytokinesis in a distribution pattern similar to that of PI4Kβ1, so we hypothesized that MAP65-3 function and/or localization might be altered in cytokinetic cells of the *pi4kβ1 pi4kβ2* double mutant. To test this hypothesis, a functional GFP-MAP65-3 fusion (Steiner *et al.*, 2016) was introgressed into the *pi4kβ1 pi4kβ2* background, and the fluorescence distribution was analyzed in root cells by live-cell time-lapse imaging (Fig 8A–C, Movies EV5 and EV6). To better assess the exact positioning of the markers in cytokinetic cells, z-stacks were recorded for each frame and used for 3D projections. The timing for both wild type and mutant is reported relative to the time point  $t_0$  when the cell plate would attach to the peripheral plasma membrane (Fig 8D). In cytokinetic cells of wild-type controls, GFP-MAP65-3 initiated at  $\sim 15$  min, and between  $\sim 12$  min and  $\sim 9$  min, the marker would undergo a transition from a disk to a ring shape (Fig 8A and C), which decorated the leading edge of the expanding cell plate (Fig 8A, Movie EV5). Beyond  $\sim 6$  min after  $t_0$ , the GFP-MAP65-3 marker would dismantle from the cell plate (Fig 8A, Movie EV5). In cytokinetic cells of the double mutant, the GFP-MAP65-3 marker initiated at  $\sim 12$  min and subsequently persisted for an extended period of time beyond 24 min after  $t_0$  (Fig 8B). The transition from a disk to a ring shape occurred in the double mutant between  $\sim 15$  min and  $\sim 18$  min (Fig 8B and C, Movie EV6), and in contrast to wild-type controls, the ring retained substantial signal in its center (Fig 8B and C, Movie EV6). Overall, prolonged disk-shaped labeling of the cell plate by GFP-MAP65-3 was displayed in cytokinetic cells of the mutant until  $t_0$  and beyond, and the marker persisted substantially into the maturation phase of the cell plate. The *in vivo* findings were further supported by immunofluorescence, and in contrast to cytokinetic wild-type cells, in which GFP-MAP65-3 formed ring-like structures during late cytokinesis (100%,  $n = 43$  cells), in cytokinetic cells of the *pi4kβ1 pi4kβ2* double mutant GFP-MAP65-3 still persisted at the center of the midline (69.4%,  $n = 121$  cells; Appendix Fig S9). Analysis of this pattern by super-resolution structured illumination microscopy (SIM) further detailed the differences in GFP-MAP65-3 distribution in 3D reconstructions (Fig 8E). While the relative timing cannot be defined with accuracy in the immunofluorescence experiments, the combined data indicate that the localization and turnover of MAP65-3 were altered in cytokinetic cells of the *pi4kβ1 pi4kβ2* double mutant. The accumulation of MAP65-3 at the midline of cytokinetic cells of the *pi4kβ1 pi4kβ2* double mutant would overstabilize noninterdigitating microtubules (nIMTs) of phragmoplasts to

### Figure 7. Disordered phragmoplast dynamics in cytokinetic root cells of the *Arabidopsis pi4kβ1 pi4kβ2* double mutant.

The dynamic transitions of phragmoplast microtubules were recorded by live-cell time-lapse imaging.

- A Five-day-old seedlings expressing mCherry-TUA5 were imaged at 1 frame per 2 min. Times are given relative to the instance when the cell plate contacted the peripheral plasma membrane, defined as  $t_0$ . Cells are outlined by dashed lines in the first and last frames of each series. White arrowhead, ectopic stabilization of microtubules in central phragmoplasts of the *pi4kβ1 pi4kβ2* double mutant. Scale bars, 10  $\mu\text{m}$ .
- B Plot profiles obtained from dashed lines marked in (A). Black arrowhead, ectopic stabilization of microtubules in central phragmoplasts of the *pi4kβ1 pi4kβ2* double mutant.
- C 3D projections from time points selected from (A), when the transition to a ring phragmoplast has occurred in wild type, but solid phragmoplast persisted in the double mutant. Scale bars, 10  $\mu\text{m}$ .
- D Duration of phragmoplast persistence during cytokinesis, determined from initiation to disbanding. \*\*\*, a significant difference ( $P < 0.001$ ) according to a two-tailed Mann–Whitney *U*-test (wild type,  $n = 12$  cells, 9 roots; *pi4kβ1 pi4kβ2*,  $n = 21$  cells, 16 roots).

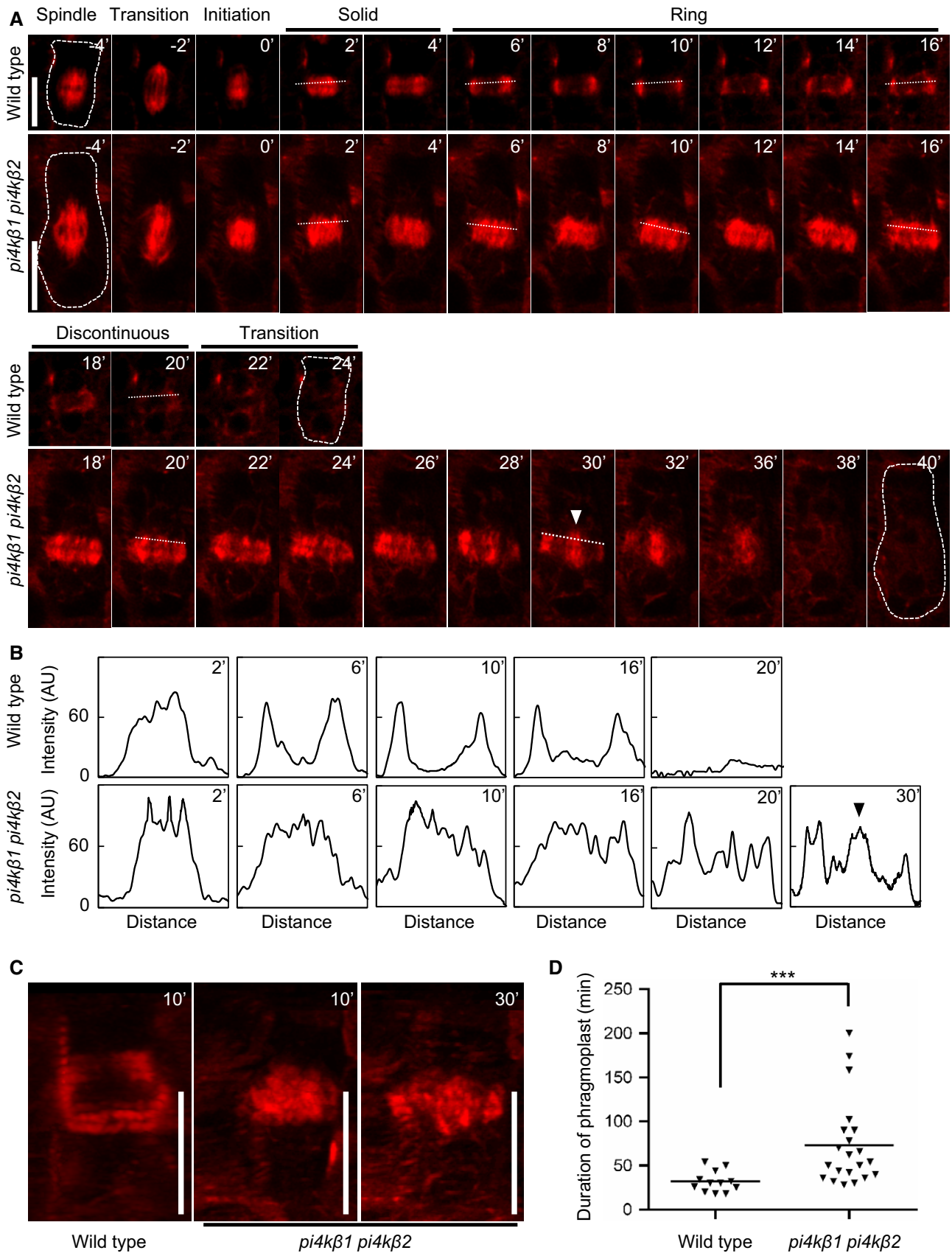


Figure 7.

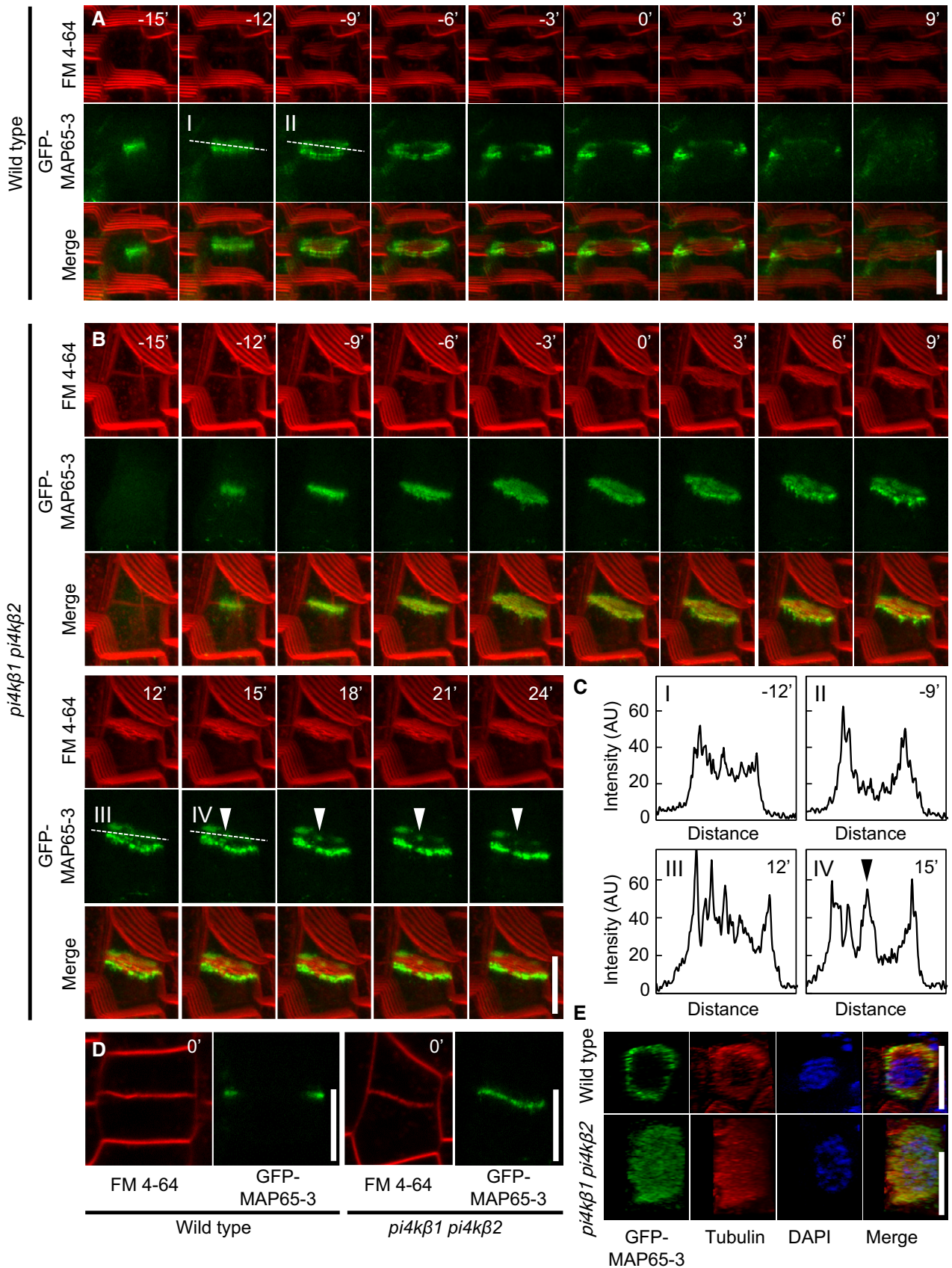


Figure 8.

**Figure 8. Mislocalization of GFP-MAP65-3 during cytokinesis in root cells of the *Arabidopsis pi4kβ1 pi4kβ2* double mutant.**

The dynamics of the microtubule bundling protein, MAP65-3, were recorded in live-cell time-lapse analyses of cytokinetic cells from root tips of wild-type controls and *pi4kβ1 pi4kβ2* double mutants.

- A Image series of 3D projections of GFP-MAP65-3 costained with FM 4-64 in root tips of 4-day-old wild-type seedlings. The best angle for visualization was obtained by rotation of the x-axis. Images are representative for 8 cells from 5 roots. Scale bar, 10 μm.
- B Image series of 3D projections of GFP-MAP65-3 costained with FM 4-64 in root tips of 4-day-old *pi4kβ1 pi4kβ2* seedlings. The best angle for visualization was obtained by rotation of the x-axis. Images are representative for 11 cells from 10 roots. Arrowheads, persisting signal of GFP-MAP65-3 in the center of the cell division plane. Scale bars, 10 μm.
- C Plot profiles were obtained from medial confocal planes at time points displaying the transition from disk to ring phragmoplasts, marked by dashed lines in (A) and (B). Arrowhead, persisting signal of GFP-MAP65-3 in the center of the cell division plane.
- D Medial confocal planes from z-stacks from (A) and (B) demonstrating attachment of the FM 4-64-stained cell plate with the peripheral plasma membrane, defining t0. Scale bars, 10 μm.
- E 3D reconstruction of ring- and disk-shaped immunofluorescence patterns for GFP-MAP65-3 and microtubules, based on super-resolution structured illumination microscopy (SIM), costained with DAPI. Top panels, wild type; bottom panels, *pi4kβ1 pi4kβ2* double mutants. Scale bars, 10 μm.

Data information: Times in (A–C) are given relative to the instance when the cell plate contacted the peripheral plasma membrane, defined as t0.

form interdigitating microtubules (IMTs), which are thought to be more stable than nIMTs (Ho *et al*, 2011), and prevent the formation of ring-like phragmoplasts, consistent with the phragmoplast patterns observed in the double mutant (cf. Fig 7). We conclude that the defective phragmoplast progression in cytokinetic cells of the *pi4kβ1 pi4kβ2* double mutant may be a consequence of mislocalized and/or dysfunctional MAP65-3, raising the question how PI4Kβ isoforms may contribute to controlling the function of MAP65-3.

#### PI4Kβ1 and the MAP65-3 regulator, MPK4, interact genetically, co-immunoprecipitate, and interact in yeast and directly *in vitro*

Three MAP65 family members (MAP65-1, MAP65-2, and MAP65-3) are well-characterized targets for phosphorylation by the MAPK, MPK4 (Sasabe *et al*, 2011). MPK4 acts in the *Arabidopsis* equivalent of the tobacco NACK-PQR pathway and is thus required for maintaining microtubule organization (Beck *et al*, 2010, 2011). Importantly, during cytokinesis MPK4 regulates the activity of MAP65-3 by phosphorylation at the cell plate (Kosetsu *et al*, 2010). As we have previously described a regulatory link between MAPKs and phosphoinositide kinases in plants (Hempel *et al*, 2017), we next asked whether similarly MPK4 is functionally linked to the role of PI4Kβs in phragmoplast progression during cytokinesis. This hypothesis is supported by the similarity of the cytokinesis phenotype of the *pi4kβ1 pi4kβ2* double mutant reported here and the cytokinesis phenotype of the *mpk4* mutant, which includes similar cytokinetic defects (Kosetsu *et al*, 2010; Beck *et al*, 2011), multinucleated cells, and stabilized microtubules (Beck *et al*, 2010). Other phenotypic similarities of the *pi4kβ1 pi4kβ2* double mutant and the *mpk4-2* mutant not related to cytokinesis have also previously been reported, including constitutive salicylic acid accumulation (Šašek *et al*, 2014; Antignani *et al*, 2015) and enhanced systemic acquired resistance (Petersen *et al*, 2000; Antignani *et al*, 2015), suggesting a functional relation between PI4Kβ isoforms and MPK4 also apart from cytokinesis. To test for a functional relation of PI4Kβ isoforms with MPK4, we first analyzed whether *PI4Kβ1* or *PI4Kβ2* genetically interacted with *MPK4*. For this purpose, the *mpk4-2* mutant was crossed with the *pi4kβ1 pi4kβ2* double mutant, and the offspring of self-pollinated *pi4kβ1<sup>-/-</sup> pi4kβ2<sup>+/-</sup> mpk4-2<sup>+/-</sup>* plants was analyzed. The overall segregation pattern obtained from these crosses (Appendix Table S1) diverged significantly from Mendelian law ( $P < 0.0001$ ). Among 181 progenies, we could not isolate a

triple homozygous plant, suggesting that fertilization, the survival of gametes, or the viability of triple homozygotes might have been affected. It is interesting to note that the *mpk4-2* allele significantly repressed the distribution of the *pi4kβ2* allele, or vice versa. The combined genotypes *pi4kβ1<sup>+/-</sup> pi4kβ2<sup>-/-</sup> mpk4-2<sup>-/-</sup>* and *pi4kβ1<sup>+/+</sup> pi4kβ2<sup>-/-</sup> mpk4-2<sup>-/-</sup>* displayed slightly reduced growth, whereas a *pi4kβ1<sup>-/-</sup> pi4kβ2<sup>+/-</sup> mpk4-2<sup>-/-</sup>* mutant was much smaller than either the *mpk4-2* or *pi4kβ1 pi4kβ2* mutants (Fig 9A). The *pi4kβ1<sup>-/-</sup> pi4kβ2<sup>+/-</sup> mpk4-2<sup>-/-</sup>* mutant displayed enhanced distortion of cell division orientation (Fig 9B). Furthermore, the proportion of multinucleated cells as well as the number of nuclei per multinucleated cell was significantly increased compared to the *mpk4-2* or *pi4kβ1 pi4kβ2* mutants ( $P < 0.001$ ), suggesting that cytokinetic defects were more pronounced (Fig 9C). As the distortion of the tissue made it difficult to identify cell wall stubs, we evaluated the proportion of KNOLLE-positive cells in the roots by immunostaining, revealing a significantly lower percentage of cytokinetic cells in the *pi4kβ1<sup>-/-</sup> pi4kβ2<sup>+/-</sup> mpk4-2<sup>-/-</sup>* mutant than in *pi4kβ1 pi4kβ2* mutants (Fig 9C). Taken together, these results suggest a synergistic genetic interaction of *PI4Kβ1* and/or *PI4Kβ2* with *MPK4*. While epistasis effects are not clear from the patterns observed, the data suggest that *in vivo* action of *MPK4* and *PI4Kβ1* and/or *PI4Kβ2* converges at a common biological process. We therefore analyzed next whether *PI4Kβ1* physically interacted with *MPK4*. For yeast two-hybrid analysis, the *PI4Kβ1* sequence was divided into two fragments, *PI4Kβ1<sub>1-566</sub>* and *PI4Kβ1<sub>422-1121</sub>*, as reported previously (Preuss *et al*, 2006). This was done, because the full-length *PI4Kβ1* has previously been shown to not interact with its partner protein, RabA4b, whereas the truncations showed positive interactions (Preuss *et al*, 2006). In these experiments, *PI4Kβ1<sub>1-566</sub>* clearly interacted with *MPK4* (Fig 10A). A positive result observed for *PI4Kβ1<sub>422-1121</sub>* cannot be interpreted, as the negative control for this fusion also gave a positive signal (Fig 10A), possibly resulting from non-specific protein binding. The interaction of *PI4Kβ1* and *MPK4* was further corroborated by co-immunoprecipitation (co-IP) from plant protein extracts (Fig 10B). Using the re-raised *PI4Kβ1* antibody, *PI4Kβ1* was detected in protein complexes immunoprecipitated from *Arabidopsis* seedlings expressing *MPK4-myc* when *MPK4-myc* was pulled down using an anti-myc antibody (Fig 10B). Please note that the large apparent size detected for the *MPK4* fusion results from the use of a previously reported functional *MPK4* fusion (Berriri *et al*, 2012), which adds nine c-Myc tags along with a polyhistidine tag and additional linker sequences. No *PI4Kβ1*

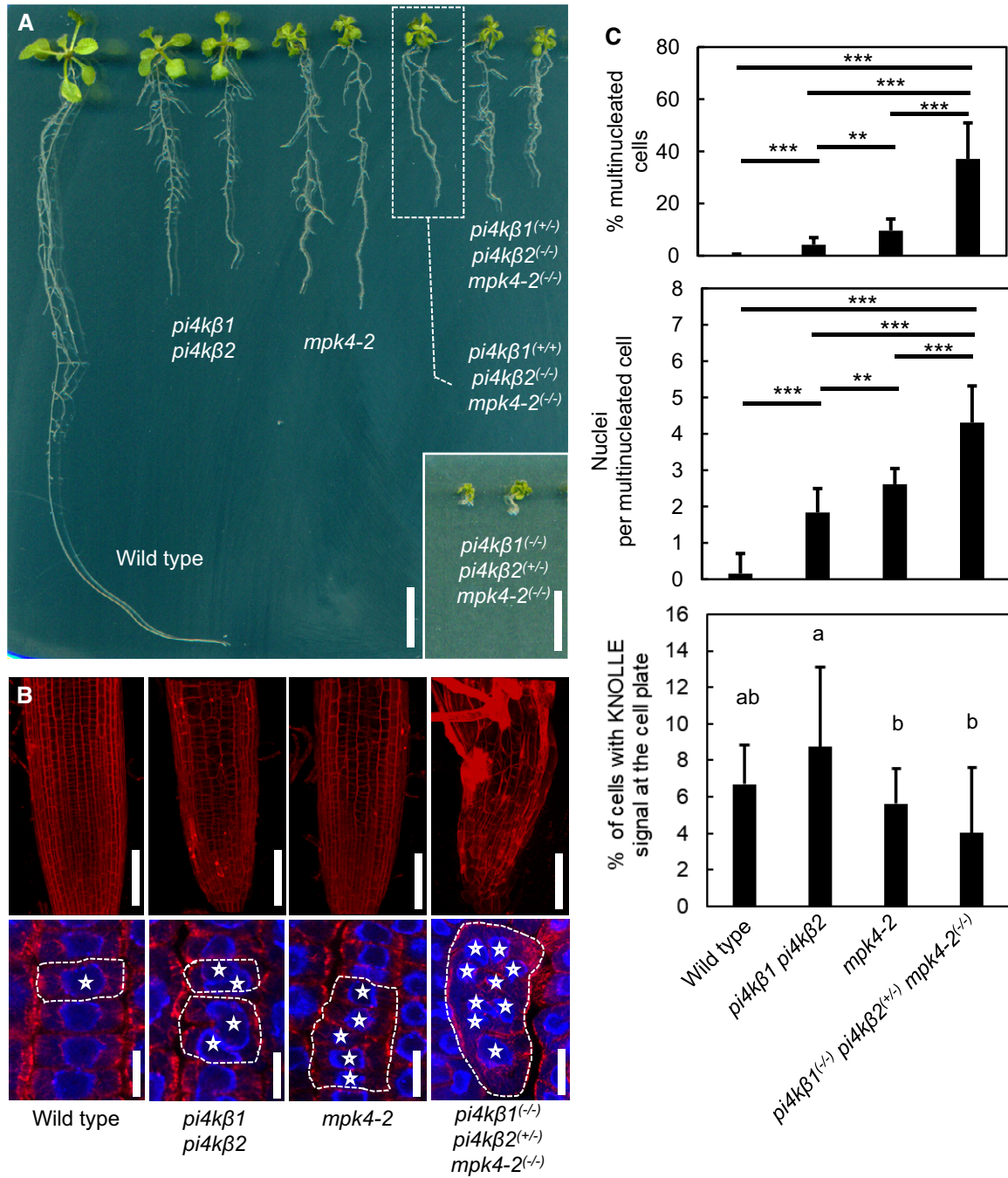


**Figure 9. Synergistic genetic interaction of Arabidopsis PI4Kβ1 and/or PI4Kβ2 with MPK4 during cytokinesis.**

The functional relations of PI4Kβ isoforms with MPK4 were tested by assessing phenotypes of crosses of the corresponding mutants.

- A** Crosses of *pi4kβ1 pi4kβ2* and *mpk4-2* mutants resulted in combined genotypes with increased growth defects, as indicated. Fourteen-day-old seedlings are shown. Scale bars, 1 cm.
- B** Top: The severe growth defects of the combined genotypes were accompanied by increased tissue distortion, as shown by 3D projections after propidium iodide staining of root tips of 14-day-old seedlings. Scale bars, 100 μm. Bottom: Multinucleation of cells was increased in the combined genotypes, as evident from immunofluorescence of microtubules (red) counterstained with DAPI (blue). Asterisks, multiple nuclei in one cell. Dashed lines indicate the outlines of exemplary multinucleated cells. Scale bars, 10 μm.
- C** Quantification of cytokinetic defects, as shown in the bottom panels of (B). Cytokinetic defects were enhanced in *pi4kβ1(-/-) pi4kβ2(+/-) mpk4-2(-/-)* (for multinucleated cells, including the percentage of multinucleated cells and the average number of nuclei in multinucleated cells, both according to a Welch ANOVA with Games-Howell post hoc test; \*\*\**P* < 0.001; \*\**P* < 0.01 (wild type, *n* = 1,650 cells, 13 roots; *pi4kβ1 pi4kβ2*, *n* = 1,441 cells, 19 roots; *mpk4-2*, *n* = 1,429 cells, 16 roots; *pi4kβ1(-/-) pi4kβ2(+/-) mpk4-2(-/-)*, *n* = 574 cells, 16 roots); and the incidence of cells displaying KNOLLE fluorescence at the cell plate according to a one-way ANOVA with post hoc Tukey HSD; *P* < 0.05, lowercase letters (wild type, *n* = 1,981 cells, 13 roots; *pi4kβ1 pi4kβ2*, *n* = 1,758 cells, 19 roots; *mpk4-2*, *n* = 1,721 cells, 16 roots; *pi4kβ1(-/-) pi4kβ2(+/-) mpk4-2(-/-)*, *n* = 660 cells, 16 roots).



signal was detected upon immunoprecipitation from wild-type seedlings used as a negative control (Fig 10B), demonstrating that the observed *in planta* association of PI4Kβ1 and MPK4 in a complex was specific. In cytokinetic *Arabidopsis* root cells, MPK4-YFP co-localized with mCherry-PI4Kβ1 at the leading edge of the growing cell plate through different cytokinetic stages (Fig 10C). Furthermore, an mRFP<sub>FAPP1-PH</sub> reporter for PtdIns(4)P also appeared synchronously with MPK4-YFP at the cell plate, albeit not concentrated at the leading edge (Fig 10D). Together the data indicate that PI4Kβ1 and MPK4 either directly interact or occur in a protein complex with functional relevance for cell plate formation in cytokinetic cells.

Based on the genetic and physical interaction of MPK4 with PI4Kβ1, we next asked whether MPK4 would influence the formation of PtdIns(4)P in cytokinetic cells. To test this hypothesis, the mRFP<sub>FAPP1-PH</sub> reporter was introgressed into the *mpk4-2* mutant background and the fluorescence intensity of the reporter was analyzed at the cell plate or the TGN (Fig 10E). In cytokinetic cells of the *mpk4-2* mutant, the ratio of cell plate-associated vs. plasma membrane fluorescence was slightly but significantly increased ( $P < 0.05$ ,  $n = 43$  cells for wild type;  $n = 32$  cells for *pi4kβ1 pi4kβ2*), indicating that MPK4 may exert an inhibitory effect on PtdIns(4)P production at the cell plate. At the same time, the reporter fluorescence at the TGN was slightly but significantly decreased (Fig 10E ( $P < 0.05$ ,  $n = 40$  cells for wild type;  $n = 32$  cell for *mpk4-2*). These experiments suggest functional interplay of MPK4 and PI4Kβ1 at the cell plate and at the TGN. While it remains to be seen whether the slight differences shown in Fig 10E are by themselves biologically relevant, MPK4 is known to regulate MAP65-3 (Kosetsu et al, 2010) in cytokinetic cells. Our combined data suggest close functional interplay of MPK4, PI4Kβ1, and MAP65-3 to control phragmoplast dynamics during somatic cytokinesis.

## Discussion

The regulatory membrane phospholipid, PtdIns(4)P, has previously been detected at the cell plate and the TGN, and the *Arabidopsis pi4kβ1 pi4kβ2* double mutant has been shown to display cytokinetic defects. However, no focused study on the functional role of PtdIns

(4)P in cell plate formation has been reported to date. Our data provide several lines of evidence for the function of PtdIns(4)P and PI4Kβ1 in cell plate formation of cytokinetic cells: a functional mCherry-PI4Kβ1 fusion localized to the cell plate *in vivo* (Fig 2); loss of *PI4Kβ1* and *PI4Kβ2* resulted in delayed recruitment of CLC2-GFP to the cell plate (Fig 4B–D), in impaired CME during cytokinesis (Fig 5A–F), in ectopically stabilized phragmoplast microtubules (Figs 6B and 7), and in mislocalized MAP65-3 (Fig 8); and the PI4Kβ pathway interacted genetically (Fig 9) and physically with the MAP65-3 regulator, MPK4 (Fig 10A and B), which furthermore influenced PtdIns(4)P formation at the cell plate (Fig 10E). In sum, our results indicate a dual role for *Arabidopsis* PI4Kβ1 in the control of membrane trafficking via influencing clathrin recruitment to the cell plate, and in the control of phragmoplast microtubules in cytokinetic cells.

Impaired membrane trafficking is consistent with the defects in cell plate formation observed in the *pi4kβ1 pi4kβ2* double mutant (cf. Figs 1 and 3). While PI4Kβs were reported to influence secretion in plants (Preuss et al, 2006; Kang et al, 2011), whether PI4Kβs were also involved in the regulation of endocytosis currently lacked evidence. Here, we found that PI4Kβs affected endocytosis in *Arabidopsis* through influencing clathrin recruitment to the cell plate of cytokinetic cells (Fig 4B–D), which is relevant for cell plate association of KNOLLE and PIN2 (Fig 5A–F). Roles of PI4Kβs in membrane trafficking, affecting both secretion and endocytosis, have also been found in animal cells (de Graaf et al, 2004; Kapp-Barnea et al, 2006; Burke et al, 2014) and yeast (Audhya et al, 2000; Yamamoto et al, 2018), suggesting PI4Kβ proteins retained functionality for regulating both secretion and endocytosis in the course of evolution. By what molecular mechanism PI4Kβs influence clathrin recruitment in *Arabidopsis* remains to be examined in the future, for instance, to elucidate the possible involvement of the adaptor proteins TPLATE or AP-2 (Di Rubbo et al, 2013; Yamaoka et al, 2013; Gadeyne et al, 2014), which recruit clathrin coats for endocytosis in *Arabidopsis*. Besides delayed recruitment of clathrin to the cell plate and to the TGN in the *pi4kβ1 pi4kβ2* double mutant, we observed altered clathrin dynamics also in interphase cells (Appendix Fig S7). Several lines of evidence support the notion that a main function of PI4Kβs is in cytokinesis, including (i) the cytokinetic phenotype of the *pi4kβ1 pi4kβ2* double mutant (Preuss et al, 2006; Kang et al, 2011); (ii) the reduced intensity of mCherry<sub>FAPP1-PH</sub>

### Figure 10. Functional association of PI4Kβ1 and MPK4 in a protein complex at the cell plate.

Experiments were performed to assess possible physical interaction, co-localization at the cell plate, and functional interplay of PI4Kβ1 and MPK4.

- PI4Kβ1 interacts with MPK4 in yeast two-hybrid tests. MPK4 was used as a bait, while PI4Kβ1 was divided into two fragments to be used as prey. The results are representative for three independent experiments.
- In vivo* co-immunoprecipitation of MPK4 and PI4Kβ1 from 14-day-old plants. PI4Kβ1 was specifically co-precipitated with MPK4-myc using anti-myc antibodies. Arrowhead, Migration of PI4Kβ1. The results are representative for three independent experiments.
- Coordination of MPK4-YFP and mCherry-PI4Kβ1 during cytokinesis in 5-day-old root meristem cells. MPK4 co-localized with PI4Kβ1 from early to late cytokinesis and gradually concentrated at the leading edges of cell plates. Images were obtained with an LSM880 in Airyscan super-resolution (SR) mode. Scale bars, 10 μm.
- Live-cell time lapse of MPK4-YFP and mRFP<sub>FAPP1-PH</sub> during cytokinesis, obtained with an LSM880 in Airyscan resolution versus sensitivity (R-S) mode. The time series is representative for six cells from five roots. Arrowheads indicate the initiation and leading edges of the growing cell plate. Scale bar, 10 μm.
- Left panels: The distribution of mRFP<sub>FAPP1-PH</sub> was observed at the cell plate at the end of cytokinesis in root meristem cells of wild-type controls (top) and *mpk4-2* mutants (bottom). Intensity profiles were recorded as indicated by the dashed lines. Scale bars, 10 μm. Right top, intensity of mRFP<sub>FAPP1-PH</sub> at the cell plate normalized vs. the intensity at the apical plasma membrane (wild type,  $n = 43$  cells, 34 roots; *mpk4-2*,  $n = 32$  cells, 28 roots). Right bottom, intensity of mRFP<sub>FAPP1-PH</sub> at the TGN normalized vs. the intensity at the apical plasma membrane (wild type,  $n = 40$  cells, 29 roots; *mpk4-2*,  $n = 26$  cells, 23 roots). \*, a significant difference ( $P < 0.05$ ) according to a two-tailed Student's test.

Source data are available online for this figure.

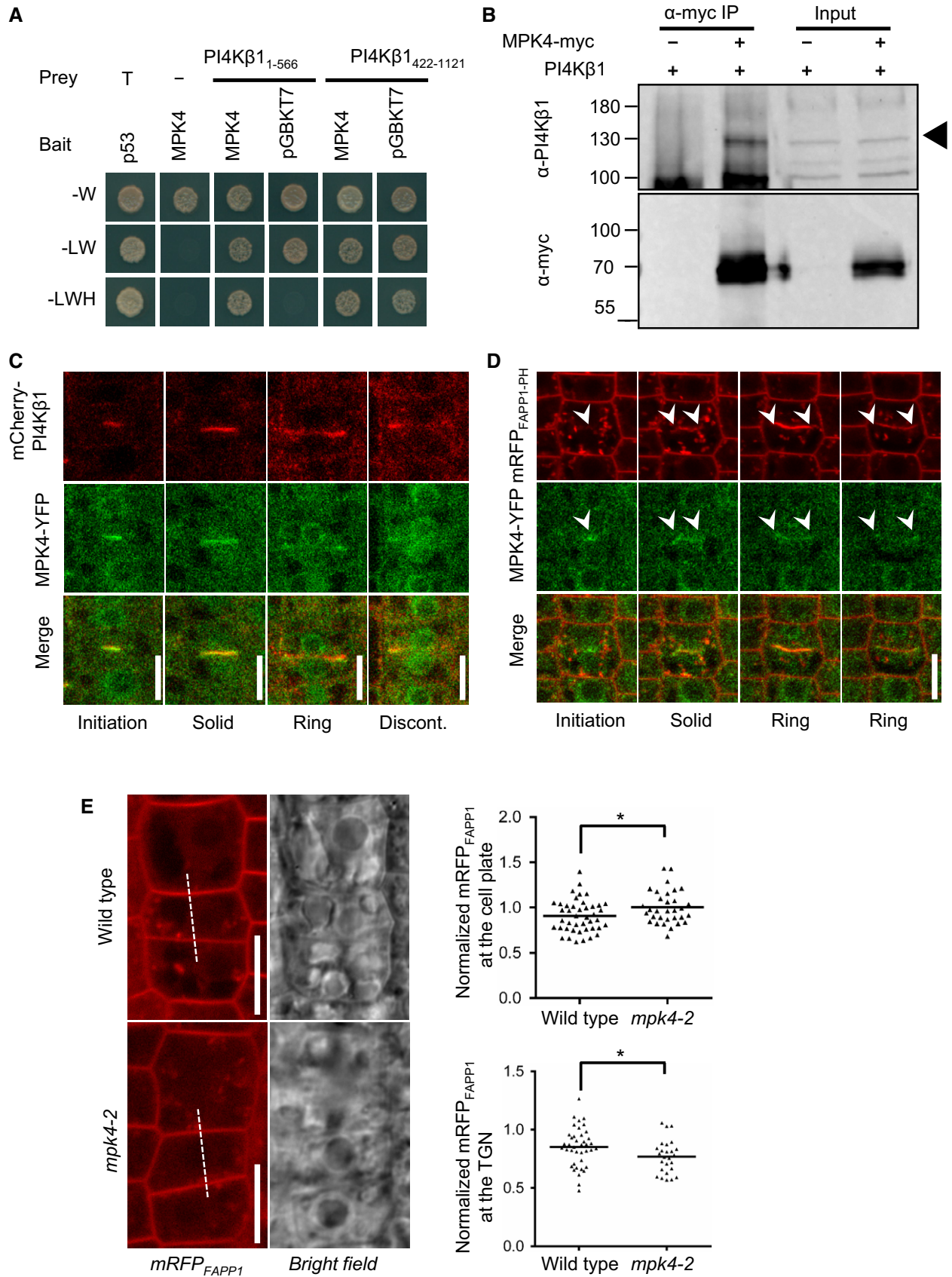


Figure 10.

at the cell plate and the TGN (Fig 4A), combined with the failure to detect changes in PtdIns(4)P levels in the *pi4kβ1 pi4kβ2* double mutant (Appendix Fig S5), which suggests a limited, localized and/or transient contribution of PI4Kβ isoforms to global PtdIns(4)P production; (iii) the delayed recruitment of CLC2-GFP to the cell plate in the mutant, based on time-lapse imaging (Fig 4B–D); (iv) the peripheral plasma membrane association of KNOLLE in the double mutant, consistent with a CME defect during cytokinesis (Fig 5A and B); and (v) the enhanced abundance of KNOLLE and PIN2 at the cell plate in the mutant (Fig 5C–F). However, it appears that PI4Kβ isoforms also play a role in membrane trafficking and microtubule organization in interphase cells, as evident from the observations that (i) expression of PI4Kβ1 from the *pKNOLLE* promoter rescued only the cytokinetic but not the root hair defects of the *pi4kβ1 pi4kβ2* double mutant (Fig 1 and Appendix Fig S1B); (ii) in the mutant the lifetime of CLC2-GFP foci at the plasma membrane of interphase cells was increased (Appendix Fig S7); (iii) the formation of PIN2-decorated BFA bodies in the mutant was reduced (Fig 5G and H); and (iv) in the mutant the internalization of FM 4–64 from the plasma membrane was reduced in interphase cells (Fig 5I and J). In sum, our data indicate a global functionality of PI4Kβ isoforms in the control of membrane trafficking at the TGN, with a predominant focus on cytokinetic cells. It is possible that in interphase cells, other PI4-kinase isoforms can partially complement the genetic lesion of the *pi4kβ1 pi4kβ2* double mutant, so that the phenotype of the double mutant is mainly the observed cytokinetic defect. While the cytokinetic defects prompted us to focus on processes at the cell plate, the production of PtdIns(4)P and the abundance of the clathrin marker CLC2-GFP were also altered at the TGN (Fig 4A and D), suggesting that PI4Kβ isoforms may influence the function of the TGN, with possible ramifications for cell plate formation.

Besides a role in membrane trafficking, we found evidence for an additional role of PI4Kβs in cytoskeletal control, because the *pi4kβ1 pi4kβ2* double mutant also displayed solid phragmoplasts at late stages of cytokinesis in cytokinetic root cells (Figs 6B and 7), indicating that the turnover of microtubules may be impaired. Further analysis showed an ectopic association of MAP65-3 protein with central areas of the maturing cell plate of cytokinetic cells (Fig 8). The depolymerization rate of microtubules was inhibited in interphase cells of the *pi4kβ1 pi4kβ2* double mutant (Appendix Fig S8), and decreased depolymerization rates are consistent with the occurrence of solid phragmoplast arrays in cytokinetic cells of these plants. Our data suggest that the defective lateral expansion of phragmoplasts in cytokinetic cells of *pi4kβ1 pi4kβ2* double mutants was a consequence of compromised regulation and/or localization of MAP65-3 during cytokinesis to overstabilize microtubules at the center of the cell plate (Fig 7A–C). The central stabilization of microtubules is relevant, because the successful transition of phragmoplast microtubular arrays from solid to ring-like structures is critical for cell plate expansion during cytokinesis (Strompen et al, 2002; Sasabe et al, 2006; Kosetsu et al, 2010). The defects in microtubule depolymerization in the *pi4kβ1 pi4kβ2* double mutants might thus be a reason for impaired lateral expansion of the phragmoplast and failing cytokinesis (Nishihama et al, 2002; Sasabe et al, 2006), similar to the effects of inhibiting microtubule depolymerization with taxol, which also hinders phragmoplast expansion (Yasuhara et al, 1993). In both *Arabidopsis* and tobacco, the activities of the MAPKs,

MPK4 (Beck et al, 2011), and NRK1 (Sasabe et al, 2006), respectively, are required for the control of phragmoplast dynamics during cytokinesis. For instance, malfunction of the HINKEL kinesin protein in the NACK-PQR pathway also induces arrest of phragmoplast expansion and results in incomplete cytokinesis and cell wall stubs (Strompen et al, 2002), similar to the effects observed in the *pi4kβ1 pi4kβ2* double mutant. It is currently unclear whether the phragmoplast defects in the *pi4kβ1 pi4kβ2* double mutant are related to the membrane trafficking defects and the altered abundance of PtdIns(4)P at the TGN (Fig 4A). It is possible that microtubules, which orient vesicles in the correct position, may not be recycled efficiently if vesicle fusion is impaired or delayed (cf. Fig 3). However, the observation of MAP65-3 mislocalization in the *pi4kβ1 pi4kβ2* double mutant (Fig 8) suggests a direct regulatory effect. While the activity of MAP65-3 is regulated at the cell plate of *Arabidopsis* cells by the NRK1 homolog, MPK4 (Kosetsu et al, 2010), our data suggest that PtdIns(4)P formation by PI4Kβ1 is required for the correct localization of MAP65-3 at the leading edge of the expanding cell plate (Fig 8). Together with the data on genetic and physical interaction of PI4Kβ1 with MPK4 (Figs 9 and 10), we are led to speculate that all three proteins might act in a cell plate-associated protein complex to regulate phragmoplast dynamics. Assuming that such a protein complex is required for correct progression of cytokinesis, then a missing partner might dissolve the complex and result in cytokinetic defects, as seen in the *mpk4-2*, *pi4kβ1 pi4kβ2*, or *map65-3* mutants. Importantly, the other partners now released from the complex might then display added functionality in their respective alternative roles, e.g., in defense. Thus, it may be that reported correlations between failed cytokinesis and salicylic acid accumulation (Šašek et al, 2014; Antignani et al, 2015) or enhanced defense (Petersen et al, 2000; Antignani et al, 2015) might be due to a functional shift of the respective PI4Kβ or MPK4 proteins toward alternative cellular roles. Future work will be directed toward elucidating the functional interrelations between the proposed protein partners of the postulated complex and their effects on phragmoplast dynamics.

As a first step to elucidate the functional interplay of MPK4 and PI4Kβ isoforms, we found increased intensity of the PtdIns(4)P reporter mRFP<sub>FAPP1-PH</sub> at the cell plate in *mpk4-2* mutants (Fig 10E) and decreased intensity of the reporter at the TGN (Fig 10E). However, the observed effects were slight and the biological significance of these observations remains currently unclear. Based on the recent report that PI4Kβ1 can be a target for phosphorylation by MPK4 (Latrasse et al, 2017), we performed a number of further experiments to delineate the molecular mechanism by which MPK4 might control PI4Kβ1 function. We could confirm this phosphorylation event *in vitro* using recombinant proteins (Appendix Fig S10A), and the modification of purified PI4Kβ1 by purified MPK4 supports a direct physical interaction of the proteins *in vitro* (cf. Fig 10). In analogy to the *in vitro* inhibition of the phosphoinositide kinase PIP5K6 by the MAPK, MPK6 (Hempel et al, 2017), we then tested the catalytic activity of PI4Kβ1 protein which had been prephosphorylated *in vitro* by MPK4, but found no change (Appendix Fig S10B). We also tested whether MPK4 exerted an effect on the subcellular localization of PI4Kβ1, but found no change in the localization of an mCherry-PI4Kβ1 marker introgressed into the *mpk4-2* mutant background (Appendix Fig S10C). As these two obvious parameters (activity or localization) of PI4Kβ1 were not influenced by MPK4, the nature of the regulatory effect of MPK4 on PI4Kβ1 appears more complex and remains to be resolved in future studies.

Here, we demonstrate the interplay of two ancient signaling pathways, the NACK-PQR pathway, and the phosphoinositide system of *Arabidopsis* in the context of membrane trafficking and somatic cytokinesis. While a role for phosphoinositides in controlling membrane trafficking has previously been shown, here we report an additional role for PtdIns(4)P in the control of microtubule dynamics, furthering our understanding of coordinated signaling pathways during somatic cytokinesis in plants and possibly other eukaryotic models.

## Materials and Methods

### Plant material, genotyping, and phenotyping

All materials used in this study were in the *Arabidopsis* Columbia background (Col-0). *pi4kβ1* (Preuss et al, 2006), *pi4kβ2* (Preuss et al, 2006), and *pi4kβ1 pi4kβ2* (Preuss et al, 2006) were used as described before. The lines PIN2-GFP (Ischebeck et al, 2013), 2×mCherry<sub>FAPP1-PH</sub> (Simon et al, 2014), GFP-MAP65-3 (Steiner et al, 2016), MPK4-YFP (Berriri et al, 2012), mCherry-TUA5 (Endler et al, 2015), mRFP<sub>FAPP1-PH</sub> (Vermeer et al, 2009), CLC2-GFP (Konopka et al, 2008), and MPK4-myc (Berriri et al, 2012) in this study have been described previously. *mpk4-2* (SALK\_056245) was obtained from the Nottingham *Arabidopsis* Stock Centre (NASC, UK). All markers were crossed into corresponding mutants, respectively, and homozygous F3 lines were used.

For genotyping of *pi4kβ1*, *pi4kβ2*, and *pi4kβ1×β2*, *pi4kβ1-LP*, GAATAGAAGCCTGCAGGAAGGG, and *pi4kβ1-RP*, AGTGCCTGTGCTTGCTATTGTCC, were used for amplification of the *PI4Kβ1* allele; *pi4kβ2-LP*, CATGGTGTACATCTCACACAATTGTC, and *pi4kβ2-RP*, GTAAAGTGCCTGTGCTGCTTGAT, were used for amplification of the *PI4Kβ2* allele; LB6316, TCAAACAGATTTTCCGCTGCT, and *pi4kβ1-RP* or *pi4kβ2-RP* were used for amplification of the *pi4kβ1* or *pi4kβ2* specific allele. Genotyping of *mpk4-2* was performed as previously described (Kosetsu et al, 2010).

### Molecular cloning and plant transformation

For genetic complementation of the *pi4kβ1 pi4kβ2* mutant, coding sequences (CDSs) of *PI4Kβ1* and *PI4Kβ2* were amplified by PCR with the following primers: *PI4Kβ1*, forward: ATGCGTGCACATGCCGATGGGACGCTTTCTAT (underlined, Sall), reverse: ATGCGGATCCTCACAAATATCCATTAAAGAC (underlined, BamHI); and *PI4Kβ2*, forward: ATGCGTGCACATGCAGATGGCACAGTTTCT (underlined, Sall), reverse: ATGCGGATCCTCATCGTATTCCATTCAACAC (underlined, BamHI). The fragments were subsequently digested and ligated into pEntry vectors. Then, 1,360-bp and 1,198-bp genomic DNA sequences upstream of start codons of *PI4Kβ1* and *PI4Kβ2* were amplified, respectively, with the following primers: *PI4Kβ1*, forward: ATGCGGCCATTACGGCCATGTTTTCTCTCACACCCTCATA (underlined, SfiI), reverse: ATGCGGCCGAGGCGGCCCTAATCAGC CAAGCATAAAAAGC (underlined, SfiI); and *PI4Kβ2*, forward: ATGCGGCCATTACGGCCAAACCGTCTGTTCTCCTCGTAA (underlined, SfiI), reverse: ATGCGGCCGAGGCGGCCCTTTGATGATCAG TCTTAGAATAA (underlined, SfiI). These two fragments were digested and ligated into pEntry vectors in front of CDSs of *PI4Kβ1* and *PI4Kβ2*, respectively, called *pPI4Kβ1-PI4Kβ1* and *pPI4Kβ2-*

*PI4Kβ2*. The FLAG tag was also introduced into the N-terminus of *PI4Kβ1* by restriction site free cloning. Then, *pPI4Kβ1-PI4Kβ1*, *pPI4Kβ2-PI4Kβ2*, and *pPI4Kβ1-FLAG-PI4Kβ1* cassettes were moved into pMDC123 binary vectors via LR reaction (Invitrogen), respectively.

For generation of *pKNOLLE-FLAG-PI4Kβ1;pi4kβ1 × β2*, 3,013 bp of *KNOLLE* cis-regulatory elements upstream of the start codon was amplified using KN-F: ATGCGGCCATTACGGCCCTTAGGATGGAGAGCCTTGCAGC (underlined, SfiI) and KN-R: ATGCGGCCGAGGCGGCCCTTTTCACCTGAAAGTCAAC (underlined, SfiI). Then, the native promoter *pPI4Kβ1* of *pPI4Kβ1-FLAG-PI4Kβ1* was excised by SfiI, and *pKNOLLE* digested by SfiI was inserted in front of the *FLAG-PI4Kβ1* cassette to produce *pKNOLLE-FLAG-PI4Kβ1*. Subsequently, *pKNOLLE-FLAG-PI4Kβ1*, which had been verified by sequencing, was transferred into the pMDC123 binary vector by LR reaction.

For *mCherry-PI4Kβ1* cloning, as genomic DNA of *PI4Kβ1* (*gPI4Kβ1*) is quite large around 11,000 bp, *mCherry-PI4Kβ1* was divided into five fragments with the following five sets of primers using RF cloning: RF-*pi4kβ1*-F1: CAACTTTGTACAAAAAGCAGGGCCTCCTTCTCAGGGAACGATGGAT, RF-*pi4kβ1*-R1: CGTCTCGCATATCTCATTAAAGCAGCCTAACTTCTCATGGCAACAGTAC; RF-*pi4kβ1*-F2: GACTGTTGCCATGGAGGAAGTTAGG, RF-*pi4kβ1*-R2: GCCAACTTTGTACAAGAAAGCTGAGTACCTGCA GAAGGTAACAGACCAAAG; RF-*pi4kβ1*-F3: CTTTGGTCTGTTACTTCTGCAGG, RF-*pi4kβ1*-R3: GCCAACTTTGTACAAGAAAGCTGAGTAGTAAACAGCGAGAGTAAACGGTAGACT; and RF-*pi4kβ1*-a1-F4: AGTCTACCGTTTACTCTCGCTGTTTAC, RF-*pi4kβ1*-R4: GCCAACTTTGTACAAGAAAGCTGAGTAGGATCCGAGTTAGTTACCGG-TAAATCAGGAGG. After assembly of whole-genomic *PI4Kβ1* into pEntry E vector, *mCherry* including a short linker SGPSC encoded by TCTGGTCCATCTGGT was amplified using the following primers: *mCherry-gPI4Kβ1*-F: GGGCTTTTATGCTTGGCTGATTAGGATGGTGAGCAAGGCGAGGAGGA, *mCherry-SGPSC-gPI4Kβ1*-R: AGATAGAAAGCGTCCCATCGGCATACCAGATGGACCAGACTTGTA CAGCTCGTCCATGCCGC (underlined, SGPSC). Then, it was fused at the N-terminus upstream of the start codon of *PI4Kβ1* via RF cloning. The construct was sequenced and moved into pMDC123 vector before transformation into *Agrobacterium* for further complementation analysis. The positive seedlings were selected with Basta and genotyped with *gPI4Kβ1-LP*: TCCAGTCCCTAGACATGATTTGTCTGTA, and *gPI4Kβ1-RP*: ATGGAAAGTTACCTGGT TGGGACC for the wild-type allele-specific fragment amplification; and LB6316: TCAAACAGATTTTCCGCTGCT and *gPI4Kβ1-RP* for the *pi4kβ1* allele-specific fragment amplification, respectively.

All vectors were transformed into *Agrobacterium tumefaciens* strain AGL0 and then transformed into *pi4kβ1 pi4kβ2* to check genetic complementation by floral dipping. Positive T1 seedlings were selected with Basta (Bayer) in soil or on 1/2 MS plates containing 10 µg/ml Phosphinothricin (Duchefa). T2 or T3 lines were used for further analyses.

### Propidium iodide staining

Five-day-old or fourteen-day-old seedlings of wild type (Col-0) and mutants were stained by propidium iodide (10 µg/ml) in H<sub>2</sub>O for 2 min, and then washed with water. The seedlings were mounted in water and immediately analyzed by confocal microscopy. We took z-stacks from surface to median section of each root with 1 µm step

size for quantification of cell wall stubs, oblique cell walls, and root meristem size. Cell wall stubs and oblique cell walls were quantified manually from all slices of z-stacks. For measurement of meristem size, the median section of propidium iodide stained root was used, and the meristem size was measured from quiescent center to the first visible elongating cell.

### Whole-mount immunostaining

Immunostaining was carried out as described before (Sauer et al, 2006) with some modifications. In brief, seedlings were fixed *in vacuo* with 4% (v/v) paraformaldehyde in PEM buffer (50 mM PIPES, pH 6.9, 1 mM EGTA, 0.5 mM MgCl<sub>2</sub>) plus 0.05% (v/v) Triton X-100 for 1 h, followed by three times of washing. The materials were partially digested using 2% (w/v) macerozyme R-10 (28302, SERVA) in PEM buffer with 0.4 M mannitol at room temperature for 30 min–1 h, with subsequent three times of washing in PEM buffer and one time of washing in PBS buffer. Samples were permeabilized with 2% (w/v) IGEPAL CA-630 and 10% (v/v) DMSO in PBS buffer for 1 h. The seedlings were washed with PBS three times and blocked with 5% (w/v) BSA in PBS for 30 min. Next, the samples were incubated with primary antibodies diluted in 3% (w/v) BSA in PBS overnight at 4°C at the required concentrations, with successive washing. Then, they were labeled with secondary antibodies diluted in 3% (w/v) BSA in PBS for 2 h at room temperature with the adequate concentrations, followed by series of washing. Finally, samples were counterstained with DAPI (1 µg/ml) for 30 min. The samples were directly mounted in PBS and immediately observed. The concentrations for primary and secondary antibodies were used as follows:

Rat monoclonal anti- $\alpha$  tubulin, clone YOL 1/34 (1:100, EMD Millipore; 1:2,000, Abcam); rabbit polyclonal anti-KNOLLE (1:4,000, provided by Prof. Gerd Jürgens, Tübingen, Germany); rabbit polyclonal anti-mCherry (1:2,000, ab167453, Abcam); rabbit polyclonal anti-GFP (1:2,000, A11122, Invitrogen). All secondary antibodies were purchased from Abcam or Invitrogen: Alexa Fluor 555 goat anti-rat IgG (H + L) (1:2,000, Abcam or Invitrogen) and Alexa Fluor 488 donkey anti-rabbit IgG (H + L) (1:2,000, Invitrogen).

For double immunostaining of ARF1 and mCherry-PI4K $\beta$ 1 in which two primary antibodies were both raised from rabbit, a modified method (Wessel & McClay, 1986) was used. Seedlings were fixed, digested, and permeabilized as described above. Then, samples were blocked with 2% (v/v) donkey serum for 30 min and then incubated with anti-ARF1 (AS08325, provided by Prof. Karin Schumacher, Heidelberg University, 1:2,000 diluted in 2% donkey serum) for 1 h at room temperature, followed by incubation with excessive goat anti-rabbit monovalent F(ab) fragments (1:20, diluted in 2% donkey serum, Jackson ImmunoResearch, Cat# 111-007-003) overnight at 4°C to convert rabbit IgG to goat IgG. Subsequently, samples were postfixated in 3.7% paraformaldehyde dissolved in PBS for 1 h, followed by blocking with 2% donkey serum for 1 h. Then, the first secondary antibodies Alexa Fluor 568 donkey anti-goat IgG (H + L) (Invitrogen) were added to samples and incubated for 2 h. Next, samples were incubated with the rabbit anti-mCherry antibodies (1:2,000, ab167453, Abcam) at 4°C overnight, followed by incubation with Alexa Fluor 488 donkey anti-rabbit IgG (H + L) (1:2,000, Invitrogen) for 2 h at room temperature. Finally, the samples were counterstained with

DAPI for 30 min. Negative controls without second primary antibodies were performed in parallel clearly showing no signal due to Alexa Fluor 488.

### Protein expression and enrichment

The CDSs of *MPK4*, *MKK6*, and *PI4K $\beta$ 1* were amplified and ligated into pGEX-4T-1 to produce GST-tagged fusion proteins, respectively. Subsequently, a constitutively active kinase MKK6<sup>DE</sup> (S221D, T227E) was generated by mutation in the Ser (S221) and Thr (T227) residues in the activation loop in MKK6. All proteins were expressed in *E. coli* BL21 (DE3). Briefly, for the GST-MPK4 and GST-MKK6<sup>DE</sup> expression, the preculture of cells was diluted into 200 ml LB liquid medium in 1:50 and allowed to grow till OD<sub>600</sub> reached 0.6–0.8 at 37°C. Then, 1 mM IPTG was added to the cell culture for protein expression for 6–8 h at 30°C. For GST-PI4K $\beta$ 1 expression, the cells were grown till OD<sub>600</sub> reached ~1.0 at 37°C. Then, 5 ml of the cells was transferred into 200 ml of LB medium filled in a 1-l flask containing 0.1 mM IPTG and incubated overnight at 25°C. Cells were harvested and purified with glutathione-Sepharose 4B beads (Thermo), following the manufacturer's instructions.

### In vitro protein phosphorylation

*In vitro* phosphorylation of proteins was assessed as described previously (Li et al, 2017). Recombinant GST-tagged MPK4 (0.3 µg) was activated by incubation with recombinant MKK6<sup>DE</sup> (0.2 µg) in the reaction buffer (30 mM Tris-HCl at pH 7.5, 10 mM MgCl<sub>2</sub>, 50 µM ATP and 1 mM DTT) at 30°C for 40 min. Activated MPK4 was then used to phosphorylate recombinant GST-PI4K $\beta$ 1 proteins (3 µg, 1:10 enzyme substrate ratio) in the same reaction buffer (30 mM Tris-HCl at pH 7.5, 10 mM MgCl<sub>2</sub>, 50 µM ATP, and 1 mM DTT) at 30°C for 30 min in the presence of 10 µCi  $\gamma$ -[<sup>32</sup>P]ATP (Hartmann Analytic GmbH, Germany). Then, all proteins were loaded into SDS-PAGE gel and processed as described above.

### In vitro lipid phosphorylation assay for PI4K $\beta$ 1 activity

The catalytic activity of PI4K $\beta$ 1 was assayed as described before (Cho & Boss, 1995). The prephosphorylated GST-PI4K $\beta$ 1 (30 µl reactions) was added to 30 µl reaction buffer to give rise to final concentrations of 30 mM Tris-HCl (pH 7.5), 1 mM cold ATP, 1 mM Na<sub>2</sub>MoO<sub>4</sub>, 15 mM MgCl<sub>2</sub>, and 10 µCi  $\gamma$ -[<sup>32</sup>P]ATP in the presence of 6 µg PtdInsP substrate presolubilized in 2% Triton X-100. Reactions were incubated at RT for 1 h. Then, the reaction was stopped by adding 1.5 ml of CHCl<sub>3</sub>:MeOH (1:2, v/v). The lipids were extracted and analyzed by thin-layer chromatography (TLC). The TLC plates were scanned by the BAS 1500 image analyzer (Fujifilm), and the intensity of phospho-labeled PtdIns(4)P was determined by using Fiji software (<https://fiji.sc/>).

### Yeast two-hybrid analysis

PI4K $\beta$ 1<sub>422-1121</sub> and PI4K $\beta$ 1<sub>1-566</sub> fragments were amplified using the following two pairs of primers: PI4K $\beta$ 1<sub>422-1121</sub>-F: ATGCCCGGG TAGGGAGGGGTTTTTCAAAAAATTC (underlined, XmaI), PI4K $\beta$ 1<sub>422-1121</sub>-R: ATGCGGATCCCTACAATATTCCATTTAAGACCC

(underlined, BamHI); and PI4K $\beta$ <sub>1-566</sub>-F: ATGCCCCGGGTATGCC GATGGGACGCTTTCTATC (underlined, XmaI), PI4K $\beta$ <sub>1-566</sub>-R: ATGCGGATCCCATATGACGTTTCACATAACGC (underlined, Bam HI). Fragments were digested and inserted into prey vectors pGADT7. The *MPK4* CDS was isolated via PCR amplification using MPK4-F: ATGCCCATGGAGATGTGGCGGAGAGTTGTTTCG (underlined, NcoI), MPK4-R: AT-GCGGATCCCTCACACTGAGTCTTGAG GATTGA (underlined, BamHI). Then, *MPK4* CDS was digested and moved into the bait vector pGBKT7. All constructs were verified by sequencing. Prey and bait vectors were co-transformed into the yeast strain Y2H Gold using a LiAc-mediated transformation protocol. Cells were selected by omitting corresponding amino acids. In order to test auto-activation, *MPK4* in bait vector pGBKT7 alone was also transformed into Y2H Gold and selected on the same media which only lacked tryptophane (Trp, W). All positive colonies were resuspended and diluted to OD<sub>600</sub> of 0.5, of which 3- $\mu$ l drops were spotted onto media lacking Trp only or Trp and leucine (Leu, L) or Trp, Leu, and histidine (His, H) to check protein interaction and auto-activation. The yeast was allowed to grow for 3 days at 30°C.

#### Generation of the rabbit anti-AtPI4K $\beta$ 1 antibody

The AtPI4K $\beta$ 1 C-terminus CTRQYDYQYRVLNGIL was synthesized (Eurogentec, Liège, Belgium) as an antigen and cross-linked to keyhole limpet hemocyanin (KLH) by an additional amino-terminal cysteine (underlined). IgG was purified from rabbit serum and affinity-purified against the column-coupled antigen (Eurogentec, Liège, Belgium). The antibody specificity was tested against protein extracts from wild type, *pi4k $\beta$ 1*, and *pi4k $\beta$ 1 pi4k $\beta$ 2* mutant plants before application in downstream experiments.

#### Co-immunoprecipitation (Co-IP) from *Arabidopsis*

For Co-IP, 14-day-old seedlings expressing functional *MPK4*-myc (Berriri *et al.*, 2012) or wild type were used. About 4–5 g material was harvested, ground with liquid nitrogen, and extracted with extraction buffer (50 mM Tris-HCl at pH 7.5, 150 mM NaCl, 1 mM EDTA, 10% glycerol, 20 mM NaF, 10 mM Na<sub>3</sub>VO<sub>4</sub>, 1 $\times$  complete protease inhibitor cocktail, 1 $\times$  PhosSTOP phosphatase inhibitor cocktail) plus 1% (w/v) Triton X-100 on ice for 1 h. Then, samples were centrifuged at 10,000 g for 30 min. Supernatants were collected and diluted with one volume extraction buffer plus 1% (w/v) Triton X-100. The same volume around 33  $\mu$ l was taken as input. After that, anti-myc antibodies (C3956, Sigma), which were bound to magnetic protein G Dynabeads (10003D, Thermo Fisher) overnight in 1 $\times$  PBS plus 0.05% (w/v) Tween-20 beforehand, were added into the supernatant and incubated at 4°C for 2.5 h with mild rotation. After incubation, beads were washed with 1 ml extraction buffer lacking NaF and Na<sub>3</sub>VO<sub>4</sub> but containing 0.1% Triton X-100 two times, and with extraction buffer without NaF, Na<sub>3</sub>VO<sub>4</sub>, and Triton X-100 three times. For final washing, beads were resuspended in the corresponding buffer and transferred into new Eppendorf tubes in order to avoid contamination coming from proteins bound to tube walls. After that, immunocomplexes were eluted with 65  $\mu$ l 2 $\times$  SDS loading buffer at 70°C for 10 min and 10  $\mu$ l was taken and loaded as IP. The proteins were subjected to SDS-PAGE gel separation and Western blotting. Primary antibodies anti-myc (1:2,000, M4439, Sigma) from mouse, anti-AtPI4K $\beta$ 1 (1:250), and all

secondary antibodies were conjugated with horseradish peroxidases (HRPs) including goat anti-mouse IgG (H + L) (A4416; Sigma) and mouse anti-rabbit IgG light chain (MAB201P; Merck Millipore). The signal was collected by a Fusion Solo S chemiluminescence imaging system (VWR) featuring a 16-bit CCD camera. The exposure time was adjusted according to the signal intensities.

#### Genetic interaction between PI4K $\beta$ 1 or PI4K $\beta$ 2 and MPK4

For analysis of genetic interaction, the *mpk4-2* allele was crossed into the *pi4k $\beta$ 1 pi4k $\beta$ 2* background, and the resulting *pi4k $\beta$ 1<sup>(+/-)</sup> pi4k $\beta$ 2<sup>(-/-)</sup> mpk4-2<sup>(+/-)</sup>* and *pi4k $\beta$ 1<sup>(-/-)</sup> pi4k $\beta$ 2<sup>(+/-)</sup> mpk4-2<sup>(+/-)</sup>* plants were analyzed. For phenotyping, seedlings were grown on half-strength solid MS medium (1% (w/v) sucrose, pH 5.6) for 14 days. After phenotyping, each seedling was genotyped. After genotyping, we noticed that 7-day-old *pi4k $\beta$ 1<sup>(-/-)</sup> pi4k $\beta$ 2<sup>(+/-)</sup> mpk4-2<sup>(-/-)</sup>* seedlings almost did not have root and had a strong phenotype. Therefore, we selected those mutants by transferring 7-day-old seedlings with “no root” to new plates allowing for another 2 days of growth (for quantification of cytokinetic defects by immunostaining). As the pattern of cell division orientation was distorted in *pi4k $\beta$ 1<sup>(-/-)</sup> pi4k $\beta$ 2<sup>(+/-)</sup> mpk4-2<sup>(-/-)</sup>*, only epidermal cells from all genotypes were counted for quantifying cytokinetic defects. We took 40 slices with 0.36  $\mu$ m step size from surface to help us clearly distinguish epidermal cells. For quantification of multinucleated cells and average number of nuclei in multinucleated cells, we quantified all nonmitotic and noncytokinetic cells.

#### Measurement of root hair length

Four-day-old seedlings grown on 1/2 MS solid plates containing 0.8% agar (Duchefa) were photographed by stereo microscopy (SteREO Discovery.V8, Carl Zeiss GmbH, Jena, Germany) equipped with an AxioCam HRC camera. Then, images were imported into Fiji and root hair length was measured manually using segmented line.

#### Confocal laser scanning microscopy (CLSM) and data analysis

All of the experiments were done with half-strength liquid MS medium (1% (w/v) sucrose, pH 5.6). Brefeldin A (BFA) and cycloheximide (CHX) were dissolved in DMSO to be 50 mM stocks, respectively. FM 4-64 was dissolved in ddH<sub>2</sub>O to be 100 mM stock. Images were acquired with LSM880 (Carl Zeiss GmbH, Jena, Germany) confocal microscopes, featuring a highly sensitive Airyscan detector (Carl Zeiss GmbH, Jena, Germany) using appropriate laser lines for excitation and emission filters for collecting signals. 20 $\times$ /N.A. 0.8 M27, 40 $\times$ /N.A. 0.95 Korr M27, or 63 $\times$ /N.A. 1.4 Oil DIC M27 oil immersion objectives were used. All images were processed with Fiji software (<https://fiji.sc/>), except images of whole-mount immunostaining, which were assembled using Adobe Photoshop.

For internalization of FM 4-64, 4-day-old seedlings were pulsed with 2  $\mu$ M FM 4-64 for 3 min on ice and then briefly washed with half-strength liquid MS medium. The seedlings were mounted with 50–100  $\mu$ l liquid MS medium in a growth chamber (ibidi, Germany) covered with 1% agarose pad, and scanned with LSM880 every 2 min until the indicated time. The images were subsequently used

for quantification of internalized FM 4-64 signal. We measured average intensity of intracellular FM 4-64 particles and average intensity of apical and basal plasma membranes. The internalized FM 4-64 was normalized to plasma membrane intensity by dividing average intracellular intensity by the average intensity of apical and basal plasma membranes.

For analysis of PIN2-GFP internalization, 5-day-old seedlings were pretreated with 50  $\mu$ M CHX for 30 min, then incubated with 50–100  $\mu$ l 25  $\mu$ M BFA and 50  $\mu$ M CHX in a growth chamber covered with 1% agarose pad, and scanned every two minutes to the indicated time points. The number of intracellular PIN2-GFP was counted manually using Fiji.

For lateral distribution of KNOLLE, 4-day-old seedlings were treated with 25  $\mu$ M BFA or without BFA for 1 h. Then, seedlings were fixed and detected as described above. The samples were observed with LSM880. The signal of cell plate-associated KNOLLE at the end of cytokinesis was measured by dividing the mean of KNOLLE at the cell plate by the mean intensity of intracellular compartments.

For measurement of PIN2-GFP at the end of cytokinesis, 5-day-old seedlings were pulsed with 2  $\mu$ M FM 4-64 for 3 min at room temperature and observed. The intensity of PIN2-GFP at the cell plate was determined by drawing a straight line across apical membrane and cell plate to acquire plot profile using Fiji. Then, the cell plate-associated PIN2-GFP intensity was normalized to the signal of apical membrane.

For quantification of 2 $\times$ mCherry<sub>FAPP1-PH</sub> at the cell plate at the end of cytokinesis, 5-day-old seedlings were imaged with LSM880 confocal microscopes. In the meantime, bright field was also taken to clearly distinguish the end of cytokinesis. The Virtual Pinhole (VP) mode was used, and images were exported using pinhole set to 2. Then, fluorescence of cell plate-associated 2 $\times$ mCherry<sub>FAPP1-PH</sub> was measured as described above for measuring PIN2-GFP at the cell plate at the end of cytokinesis. The intensity was also normalized to the intensity of the apical plasma membrane.

For quantification of mRFP<sub>FAPP1-PH</sub> in *mpk4-2*, 4-day-old seedlings were imaged using a gallium arsenide phosphide (GaAsP) detector. The fluorescence of at the cell plate at the end of cytokinesis was measured and normalized as described above for quantification of 2 $\times$ mCherry<sub>FAPP1-PH</sub> at the cell plate at the end of cytokinesis.

For time-lapse imaging of GFP-MAP65-3 or CLC2-GFP, 5-day-old seedlings were stained with 2  $\mu$ M FM 4-64 for 3 min at room temperature and washed with liquid MS medium. The seedlings were mounted in 50–100  $\mu$ l MS medium covered with a 1% agarose pad in growth chamber and imaged. Seven to eleven slices of z-stacks with 1  $\mu$ m step size to cover median sections of cells were taken, and images were taken every 3 min in order to avoid bleaching. Movies EV1–EV6 were recorded using the macro Correct\_3D\_Drift\_Plus (<https://github.com/tischi/fiji-correct-3d-drift>). For GFP-MAP65-3 dynamics, the Movies EV1–EV6 were projected with “3D project” in Fiji for each time point with 10° increments of rotation at *x*-axis to acquire 4D resolution of Movies EV1–EV6, and the best angle for visualizing 3D at the cell plate was selected manually. For CLC2-GFP recruitment to the cell plate, the slice which is close to the median section was selected manually and reconstructed. For quantification of delayed events of CLC2-GFP recruitment in the mutants, the time point when the cell plate had just attached with

the plasma membrane was set to time “0”. In this case, any recruitment of CLC2-GFP before the cell plate fusion with plasma membrane would give minus values. By contrast, plus values mean recruitment of CLC2-GFP to the cell plate after the cell plate fusion with the plasma membrane.

For time-lapse imaging of MPK4-YFP  $\times$  mRFP<sub>FAPP1-PH</sub> dual markers, images were taken using the LSM880. As MPK4-YFP signal is weak, we used the highly sensitive Airyscan detector to take images. In this case, laser intensity was reduced to 1% to enable long-term imaging and to avoid bleaching. The interval was set to 90 s, and resolution vs. sensitivity (R-S) mode of Airyscan was used. The Movies EV1–EV6 were also recorded using the macro Correct\_3D\_Drift\_Plus.

For the mCherry-PI4K $\beta$ 1 or mCherry-PI4K $\beta$ 1  $\times$  MPK4-YFP marker lines, the VP or super-resolution (SR) mode of the Airyscan detector was used, and the pinhole for image output was set to 2 in case VP mode was used.

### Spinning disk microscopy and data analysis

Images were taken by Zeiss Cell Observer SD microscope equipped with a Yokogawa CSU-X1 spinning disk head. A 100 $\times$  oil immersion objective and a Photometrics Evolve 512 Delta EM-CCD camera were used to acquire images. GFP and mCherry were excited at 488 nm and 561 nm, respectively, and a DBP 527/54+645/60 band-pass emission filter (Chroma Technology) was used. For imaging of microtubule dynamics, a 5-s interval was used to acquire time-lapse images, while CLC2-GFP was imaged every 2 s. Images were contrast-enhanced, background-subtracted, registered, and walking averaged. For quantifying the velocity of microtubules, a Java macro was then used to separate growing and shrinking ends by time phase to phase subtraction (Endler *et al*, 2015). The plugin MultiKymograph ([https://www.embl.de/eamnet/html/body\\_kymograph.html](https://www.embl.de/eamnet/html/body_kymograph.html)) was used to generate kymographs for measurement of velocities of growth and shrinkage and lifetime.

### Super-resolution microscopy

To analyze the ultrastructure of immunostains beyond the classical Abbe/Raleigh limit at a lateral resolution of  $\sim$ 120 nm (super-resolution, achieved with a 488-nm laser), a spatial 3D-structured illumination microscopy (3D-SIM) was applied using a 63 $\times$ 1.4NA Oil Plan-Apochromat objective of an Elyra PS.1 microscope system and the software ZEN black was used to capture images (Carl Zeiss GmbH; Weissart *et al*, 2016). Images were captured separately for each fluorochrome using the 561-, 488-, and 405-nm laser lines for excitation and appropriate emission filters. 3D rendering based on SIM image stacks was done using the Imaris 8.0 (Bit-plane) software.

### Transmission electron microscopy

The material was prepared for histological and ultrastructural investigations as previously described (Behr *et al*, 2010). In brief, the material was fixed with 3% glutaraldehyde (Sigma) in 0.1 M sodium cacodylate buffer (pH 7.2) (SCB), washed, postfixed with 1% osmium tetroxide (Carl Roth, Karlsruhe, Germany) in SCB, dehydrated in a graded series of ethanol, and embedded in epoxy

resin as previously described (Spurr, 1969). Ultrathin sections (80 nm) were observed with an EM 900 (Carl Zeiss Microscopy, Jena, Germany) transmission electron microscope (acceleration voltage 80 kV). Electron micrographs were taken with a slow scan camera (Variospeed SSCCD camera SM-1k-120, TRS, Moorenweis, Germany) using the iTEM software from Olympus SIS (Münster, Germany).

### Extraction and quantification of PtdIns(4)P

Lipid extraction was performed using an acidic lipid extraction method to allow quantification of anionic lipids (König *et al*, 2008) with slight modifications. The samples were analyzed using a 30 m × 250 μm DB-23 capillary column (Agilent) and a GC-2010 Plus GC/FID system (Shimadzu). The lipid amount was quantified by using the internal control and normalized against the sample fresh weight.

### Statistical analysis

We used PASW Statistics (SPSS) 18 to evaluate the homogeneity of variance. The significance was then determined by independent-samples two-tailed *t*-test or one-way ANOVA or Mann–Whitney *U*-test. The Excel software (Microsoft) was used to create bar charts, and GraphPad software was used to create cloud plots.

**Expanded View** for this article is available online.

### Acknowledgements

We would like to thank Dr. Erik Nielsen (University of Michigan, Ann Arbor, MI, USA) and Dr. Eric Ruelland (CNRS, Paris, France) for providing the published *pi4kβ1*, *pi4kβ2* and *pi4kβ1 pi4kβ2* mutants. We are grateful to Prof. Gerd Jürgens (University of Tübingen, Germany) and to Prof. Karin Schumacher (Centre for Organismic Studies, University of Heidelberg, Germany) for providing the KNOLLE and ARF1 antibodies, respectively, and to Prof. Farhah F. Assaad (Technische Universität München, Germany) and Prof. Marie-Theres Hauser (University of Natural Resources and Life Sciences, Vienna (BOKU), Austria) for the GFP-MAP65-3 marker line. We thank Dr. Jean Colcombet (Université Paris-Sud, INRA, France) for kindly sharing the MPK4-YFP, MPK4-myc lines. We also would like to thank Prof. Staffan Persson and Dr. Rene Schneider (University of Melbourne, VIC, AU) for providing the mCherry-TUA5 line and a Fiji macro to analyze microtubule dynamics. We also thank Prof. Bettina Hause and Dr. Justin Lee (both Leibniz Institute of Plant Biochemistry, Halle, Germany) for sharing space for plant growth and for the *MPK4* cDNA clone, respectively, and Prof. Kirsten Bacia (Martin-Luther-University Halle-Wittenberg) for access to the spinning disk microscope. We gratefully acknowledge generous financial support from the German Research Foundation (DFG, Grant He3424/6; CRC648 TP B10; and INST271/371-1 FUGG to I.H.; and TP Z1 to G.H.) and a PhD scholarship from the Chinese Scholarship Council (CSC 201306850014 to F.L.).

### Author contributions

FL, PK, and IH designed research; FL, PK, VS, GH, and MH performed experiments; FL, PK, VS, GH, MH, and IH analyzed data; and FL and IH wrote the manuscript.

### Conflict of interest

The authors declare that they have no conflict of interest.

## References

- Antignani V, Klocko AL, Bak G, Chandrasekaran SD, Dunivin T, Nielsen E (2015) Recruitment of PLANT U-BOX13 and the PI4Kβ1/β2 phosphatidylinositol-4 kinases by the small GTPase Raba4B plays important roles during salicylic acid-mediated plant defense signaling in *Arabidopsis*. *Plant Cell* 27: 243–261
- Audhya A, Foti M, Emr SD (2000) Distinct roles for the yeast phosphatidylinositol 4-Kinases, Stt4p and Pik1p, in secretion, cell growth, and organelle membrane dynamics. *Mol Biol Cell* 11: 2673–2689
- Balla T, Bondeva T, Varnai P (2000) How accurately can we image inositol lipids in living cells? *Trends Pharmacol Sci* 21: 238–241
- Beck M, Komis G, Müller J, Menzel D, Šamaj J (2010) *Arabidopsis* homologs of nucleus- and phragmoplast-localized kinase 2 and 3 and mitogen-activated protein kinase 4 are essential for microtubule organization. *Plant Cell* 22: 755–771
- Beck M, Komis G, Ziemann A, Menzel D, Šamaj J (2011) Mitogen-activated protein kinase 4 is involved in the regulation of mitotic and cytokinetic microtubule transitions in *Arabidopsis thaliana*. *New Phytol* 189: 1069–1083
- Behr M, Humbeck K, Hause G, Deising HB, Wirsal SGR (2010) The hemibiotroph colletotrichum graminicola locally induces photosynthetically active green islands but globally accelerates senescence on aging maize leaves. *Mol Plant Microbe Interact* 23: 879–892
- Berriri S, Garcia AV, dit Frey NF, Rozhon W, Pateyron S, Leonhardt N, Montillet J-L, Leung J, Hirt H, Colcombet J (2012) Constitutively active mitogen-activated protein kinase versions reveal functions of *Arabidopsis* MPK4 in pathogen defense signaling. *Plant Cell* 24: 4281–4293
- Boutté Y, Frescatada-Rosa M, Men S, Chow CM, Ebine K, Gustavsson A, Johansson L, Ueda T, Moore I, Jürgens G, Grebe M (2010) Endocytosis restricts *Arabidopsis* KNOLLE syntaxin to the cell division plane during late cytokinesis. *EMBO J* 29: 546–558
- Burke JE, Inglis AJ, Perisic O, Masson GR, McLaughlin SH, Rutaganira F, Shokat KM, Williams RL (2014) Structures of PI4KIIIβ complexes show simultaneous recruitment of Rab11 and its effectors. *Science* 344: 1035–1038
- Cho MH, Boss WF (1995) Transmembrane signaling and phosphoinositides. In *Methods in Cell Biology*, Galbraith DW, Bohnert HJ, Bourque DP (eds), Vol. 49, pp 543–554. Amsterdam: Elsevier
- D'Avino PP, Savoian MS, Glover DM (2005) Cleavage furrow formation and ingression during animal cytokinesis: a microtubule legacy. *J Cell Sci* 118: 1549–1558
- Di Rubbo S, Irani NG, Kim SY, Xu Z-Y, Gadeyne A, Dejonghe W, Vanhoutte I, Persiau G, Eeckhout D, Simon S, Song K, Kleine-Vehn J, Friml J, De Jaeger G, Van Damme D, Hwang I, Russinova E (2013) The clathrin adaptor complex AP-2 mediates endocytosis of brassinosteroid insensitive1 in *Arabidopsis*. *Plant Cell* 25: 2986–2997
- Endler A, Kesten C, Schneider R, Zhang Y, Ivakov A, Froehlich A, Funke N, Persson S (2015) A mechanism for sustained cellulose synthesis during salt stress. *Cell* 162: 1353–1364
- Gadeyne A, Sánchez-Rodríguez C, Vanneste S, Di Rubbo S, Zauber H, Vanneste K, Van Leene J, De Winne N, Eeckhout D, Persiau G, Van De Slijke E, Cannoot B, Vercruyse L, Mayers Jonathan R, Adamowski M, Kania U, Ehrlich M, Schweighofer A, Ketelaar T, Maere S *et al* (2014) The TPLATE adaptor complex drives clathrin-mediated endocytosis in plants. *Cell* 156: 691–704
- Gerth K, Lin F, Menzel W, Krishnamoorthy P, Stenzel I, Heilmann M, Heilmann I (2017) Guilt by association: a phenotype-based view of the plant phosphoinositide network. *Annu Rev Plant Biol* 68: 349–374



- Gloor Y, Schöne M, Habermann B, Ercan E, Beck M, Weselek G, Müller-Reichert T, Walch-Solimena C (2010) Interaction between Sec7p and Pik1p: the first clue for the regulation of a coincidence detection signal. *Eur J Cell Biol* 89: 575–583
- Glotzer M (2001) Animal cell cytokinesis. *Annu Rev Cell Dev Biol* 17: 351–386
- Godi A, Di Campi A, Konstantakopoulos A, Di Tullio G, Alessi DR, Kular GS, Daniele T, Marra P, Lucocq JM, De Matteis MA (2004) FAPPs control Golgi-to-cell-surface membrane traffic by binding to ARF and PtdIns(4)P. *Nat Cell Biol* 6: 393–404
- de Graaf P, Zwart WT, van Dijken RA, Deneka M, Schulz TK, Geijsen N, Coffey PJ, Gadella BM, Verkleij AJ, van der Sluijs P (2004) Phosphatidylinositol 4-kinase $\beta$  is critical for functional association of rab11 with the Golgi complex. *Mol Biol Cell* 15: 2038–2047
- He J, Scott JL, Heroux A, Roy S, Lenoir M, Overduin M, Stahelin RV, Kutateladze TG (2011) Molecular basis of phosphatidylinositol 4-phosphate and ARF1 GTPase recognition by the FAPP1 pleckstrin homology (PH) domain. *J Biol Chem* 286: 18650–18657
- Heilmann I (2016) Phosphoinositide signaling in plant development. *Development* 143: 2044–2055
- Hempel F, Stenzel I, Heilmann M, Krishnamoorthy P, Menzel W, Golbik R, Helm S, Dobritzsch D, Baginsky S, Lee J, Hoehenwarter W, Heilmann I (2017) MAPKs influence pollen tube growth by controlling the formation of phosphatidylinositol 4,5-bisphosphate in an apical plasma membrane domain. *Plant Cell* 29: 3030–3050
- Ho C-MK, Hotta T, Guo F, Roberson RW, Lee Y-RJ, Liu B (2011) Interaction of antiparallel microtubules in the phragmoplast is mediated by the microtubule-associated protein MAP65-3 in *Arabidopsis*. *Plant Cell* 23: 2909–2923
- Ischebeck T, Werner S, Krishnamoorthy P, Lerche J, Meijón M, Stenzel I, Löffke C, Wiessner T, Im YJ, Perera IY, Iven T, Feussner I, Busch W, Boss WF, Teichmann T, Hause B, Persson S, Heilmann I (2013) Phosphatidylinositol 4,5-bisphosphate influences PIN polarization by controlling clathrin-mediated membrane trafficking in *Arabidopsis*. *Plant Cell* 25: 4894–4911
- Ito E, Fujimoto M, Ebine K, Uemura T, Ueda T, Nakano A (2012) Dynamic behavior of clathrin in *Arabidopsis thaliana* unveiled by live imaging. *Plant J* 69: 204–216
- Jürgens G (2005) Plant cytokinesis: fission by fusion. *Trends Cell Biol* 15: 277–283
- Kang BH, Nielsen E, Preuss ML, Mastronarde D, Staehelin LA (2011) Electron tomography of RabA4b- and PI-4K $\beta$ 1-labeled trans golgi network compartments in *Arabidopsis*. *Traffic* 12: 313–329
- Kapp-Barnea Y, Ninio-Many L, Hirschberg K, Fukuda M, Jeromin A, Sagi-Eisenberg R, Gruenberg J (2006) Neuronal calcium sensor-1 and phosphatidylinositol 4-kinase  $\beta$  stimulate extracellular signal-regulated kinase 1/2 signaling by accelerating recycling through the endocytic recycling compartment. *Mol Biol Cell* 17: 4130–4141
- König S, Hoffmann M, Mosblech A, Heilmann I (2008) Determination of content and fatty acid composition of unlabeled phosphoinositide species by thin-layer chromatography and gas chromatography. *Anal Biochem* 378: 197–201
- Konopka CA, Backues SK, Bednarek SY (2008) Dynamics of *Arabidopsis* dynamin-related protein 1C and a clathrin light chain at the plasma membrane. *Plant Cell* 20: 1363–1380
- Kosetsu K, Matsunaga S, Nakagami H, Colcombet J, Sasabe M, Soyano T, Takahashi Y, Hirt H, Machida Y (2010) The MAP kinase MPK4 is required for cytokinesis in *Arabidopsis thaliana*. *Plant Cell* 22: 3778–3790
- Latrasse D, Jégu T, Li H, de Zelicourt A, Raynaud C, Legras S, Gust A, Samajova O, Veluchamy A, Rayapuram N, Ramirez-Prado JS, Kulikova O, Colcombet J, Bigeard J, Genot B, Bisseling T, Benhamed M, Hirt H (2017) MAPK-triggered chromatin reprogramming by histone deacetylase in plant innate immunity. *Genome Biol* 18: 131
- Li H, Ding Y, Shi Y, Zhang X, Zhang S, Gong Z, Yang S (2017) MPK3- and MPK6-Mediated ICE1 phosphorylation negatively regulates ICE1 stability and freezing tolerance in *Arabidopsis*. *Dev Cell* 43: 630–642.e634
- Liu Y, Kahn RA, Prestegard JH (2014) Interaction of Fapp1 with Arf1 and PI4P at a membrane surface: an example of coincidence detection. *Structure* 22: 421–430
- Lucas JR, Shaw SL (2012) MAP65-1 and MAP65-2 promote cell proliferation and axial growth in *Arabidopsis* roots. *Plant J* 71: 454–463
- McMichael CM, Bednarek SY (2013) Cytoskeletal and membrane dynamics during higher plant cytokinesis. *New Phytol* 197: 1039–1057
- Mueller-Roeber B, Pical C (2002) Inositol phospholipid metabolism in *Arabidopsis*. Characterized and putative isoforms of inositol phospholipid kinase and phosphoinositide-specific phospholipase C. *Plant Physiol* 130: 22–46
- Muller I, Wagner W, Volker A, Schellmann S, Nacry P, Kuttner F, Schwarz-Sommer Z, Mayer U, Jürgens G (2003) Syntaxin specificity of cytokinesis in *Arabidopsis*. *Nat Cell Biol* 5: 531–534
- Müller S, Smertenko A, Wagner V, Heinrich M, Hussey PJ, Hauser M-T (2004) The plant microtubule-associated protein AtMAP65-3/PLE is essential for cytokinetic phragmoplast function. *Curr Biol* 14: 412–417
- Müller S, Jürgens G (2016) Plant cytokinesis—No ring, no constriction but centrifugal construction of the partitioning membrane. *Semin Cell Dev Biol* 53: 10–18
- Munnik T, Nielsen E (2011) Green light for polyphosphoinositide signals in plants. *Curr Opin Plant Biol* 14: 489–497
- Murata T, Sano T, Sasabe M, Nonaka S, Higashiyama T, Hasezawa S, Machida Y, Hasebe M (2013) Mechanism of microtubule array expansion in the cytokinetic phragmoplast. *Nat Commun* 4: 1967
- Nishihama R, Machida Y (2001) Expansion of the phragmoplast during plant cytokinesis: a MAPK pathway may MAP it out. *Curr Opin Plant Biol* 4: 507–512
- Nishihama R, Soyano T, Ishikawa M, Araki S, Tanaka H, Asada T, Irie K, Ito M, Terada M, Banno H, Yamazaki Y, Machida Y (2002) Expansion of the cell plate in plant cytokinesis requires a kinesin-like protein/MAPKKK complex. *Cell* 109: 87–99
- Petersen M, Brodersen P, Naested H, Andreasson E, Lindhart U, Johansen B, Nielsen HB, Lacy M, Austin MJ, Parker JE, Sharma SB, Klessig DF, Martienssen R, Mattsson O, Jensen AB, Mundy J (2000) *Arabidopsis* MAP kinase 4 negatively regulates systemic acquired resistance. *Cell* 103: 1111–1120
- Preuss ML, Schmitz AJ, Thole JM, Bonner HKS, Otegui MS, Nielsen E (2006) A role for the RabA4b effector protein PI-4K $\beta$ 1 in polarized expansion of root hair cells in *Arabidopsis thaliana*. *J Cell Biol* 172: 991–998
- Reichardt I, Stierhof Y-D, Mayer U, Richter S, Schwarz H, Schumacher K, Jürgens G (2007) Plant cytokinesis requires *de novo* secretory trafficking but not endocytosis. *Curr Biol* 17: 2047–2053
- Sasabe M, Soyano T, Takahashi Y, Sonobe S, Igarashi H, Itoh TJ, Hidaka M, Machida Y (2006) Phosphorylation of NtMAP65-1 by a MAP kinase down-regulates its activity of microtubule bundling and stimulates progression of cytokinesis of tobacco cells. *Genes Dev* 20: 1004–1014
- Sasabe M, Kosetsu K, Hidaka M, Murase A, Machida Y (2011) *Arabidopsis thaliana* MAP65-1 and MAP65-2 function redundantly with MAP65-3/PLEIADE in cytokinesis downstream of MPK4. *Plant Signal Behav* 6: 743–747
- Sasabe M, Machida Y (2012) Regulation of organization and function of microtubules by the mitogen-activated protein kinase cascade during plant cytokinesis. *Cytoskeleton* 69: 913–918

- Šašek V, Janda M, Delage E, Puyaubert J, Guivarc'h A, López Masada E, Dobrev PI, Caius J, Bóka K, Valentová O, Burketová L, Zachowski A, Ruelland E (2014) Constitutive salicylic acid accumulation in pi4klil1β1β2 *Arabidopsis* plants stunts rosette but not root growth. *New Phytol* 203: 805–816
- Sauer M, Paciorek T, Benkova E, Friml J (2006) Immunocytochemical techniques for whole-mount *in situ* protein localization in plants. *Nat Protoc* 1: 98–103
- Seguí-Simarro JM, Austin JR, White EA, Staehelin LA (2004) Electron tomographic analysis of somatic cell plate formation in meristematic cells of *Arabidopsis* preserved by high-pressure freezing. *Plant Cell* 16: 836–856
- Simon MLA, Platre MP, Assil S, Wijk R, Chen WY, Chory J, Dreux M, Munnik T, Jaillais Y (2014) A multi-colour/multi-affinity marker set to visualize phosphoinositide dynamics in *Arabidopsis*. *Plant J* 77: 322–337
- Simon MLA, Platre MP, Marqués-Bueno MM, Armengot L, Stanislas T, Bayle V, Caillaud M-C, Jaillais Y (2016) A PtdIns(4)P-driven electrostatic field controls cell membrane identity and signalling in plants. *Nat Plants* 2: 16089
- Smertenko A, Assaad F, Baluška F, Bezanilla M, Buschmann H, Drakakaki G, Hauser M-T, Janson M, Mineyuki Y, Moore I, Müller S, Murata T, Otegui MS, Panteris E, Rasmussen C, Schmit A-C, Šamaj J, Samuels L, Staehelin LA, Van Damme D et al (2017a) Plant cytokinesis: terminology for structures and processes. *Trends Cell Biol* 27: 885–894
- Smertenko A, Hewitt SL, Jacques CN, Kacprzyk R, Liu Y, Marcec MJ, Moyo L, Ogden A, Oung HM, Schmidt S, Serrano-Romero EA (2017b) Phragmoplast microtubule dynamics – a game of zones. *J Cell Sci* 131: jcs203331
- Soyano T, Nishihama R, Morikiyo K, Ishikawa M, Machida Y (2003) NQK1/NtMEK1 is a MAPKK that acts in the NPK1 MAPKKK-mediated MAPK cascade and is required for plant cytokinesis. *Genes Dev* 17: 1055–1067
- Spurr AR (1969) A low-viscosity epoxy resin embedding medium for electron microscopy. *J Ultrastruct Res* 26: 31–43
- Steiner A, Müller L, Rybak K, Vodermaier V, Facher E, Thellmann M, Ravikumar R, Wanner G, Hauser M-T, Assaad Farhah F (2016) The membrane-associated Sec1/Munc18 KEULE is required for phragmoplast microtubule reorganization during cytokinesis in *Arabidopsis*. *Mol Plant* 9: 528–540
- Strompen G, El Kasmi F, Richter S, Lukowitz W, Assaad FF, Jürgens G, Mayer U (2002) The *Arabidopsis* HINKEL gene encodes a kinesin-related protein involved in cytokinesis and is expressed in a cell cycle-dependent manner. *Curr Biol* 12: 153–158
- Takahashi Y, Soyano T, Kosetsu K, Sasabe M, Machida Y (2010) HINKEL kinesin, ANP MAPKKs and MKK6/ANQ MAPKK, which phosphorylates and activates MPK4 MAPK, constitute a pathway that is required for cytokinesis in *Arabidopsis thaliana*. *Plant and Cell Physiology* 51: 1766–1776
- Tanaka H, Ishikawa M, Kitamura S, Takahashi Y, Soyano T, Machida C, Machida Y (2004) The AtNACK1/HINKEL and STUD/TETRASPORE/AtNACK2 genes, which encode functionally redundant kinesins, are essential for cytokinesis in *Arabidopsis*. *Genes to Cells* 9: 1199–1211
- Varnai P, Balla T (2008) Live cell imaging of phosphoinositides with expressed inositide binding protein domains. *Methods* 46: 167–176
- Vermeer JEM, Thole JM, Goedhart J, Nielsen E, Munnik T, Gadella TWJ Jr (2009) Imaging phosphatidylinositol 4-phosphate dynamics in living plant cells. *Plant J* 57: 356–372
- Viotti C, Bubeck J, Stierhof Y-D, Krebs M, Langhans M, van den Berg W, van Dongen W, Richter S, Geldner N, Takano J, Jürgens G, de Vries SC, Robinson DG, Schumacher K (2010) Endocytic and secretory traffic in *Arabidopsis* merge in the trans-golgi network/Early endosome, an independent and highly dynamic organelle. *Plant Cell* 22: 1344–1357
- Weisshart K, Fuchs J, Schubert V (2016) Structured illumination microscopy (SIM) and photoactivated localization microscopy (PALM) to analyze the abundance and distribution of RNA Polymerase II molecules on flow-sorted *Arabidopsis* nuclei. *Bio Protoc* 6: e1725
- Wessel GM, McClay DR (1986) Two embryonic, tissue-specific molecules identified by a double-label immunofluorescence technique for monoclonal antibodies. *J Histochem Cytochem* 34: 703–706
- Yamamoto W, Wada S, Nagano M, Aoshima K, Siekhaus DE, Toshima JY, Toshima J (2018) Distinct roles for plasma membrane PtdIns(4)P and PtdIns(4,5)P<sub>2</sub> during receptor-mediated endocytosis in yeast. *J Cell Sci* 131: jcs207696
- Yamaoka S, Shimono Y, Shirakawa M, Fukao Y, Kawase T, Hatsugai N, Tamura K, Shimada T, Hara-Nishimura I (2013) Identification and dynamics of *Arabidopsis* adaptor protein-2 complex and its involvement in floral organ development. *Plant Cell* 25: 2958–2969
- Yasuhara H, Sonobe S, Shibaoka H (1993) Effects of taxol on the development of the cell plate and of the phragmoplast in tobacco by-2 cells. *Plant Cell Physiol* 34: 21–29